Acta Pharmaceutica Sinica B 2026;16(3):1466−1488

Chinese Pharmaceutical Association
Institute of Materia Medica, Chinese Academy of Medical Sciences

Acta Pharmaceutica Sinica B

www.elsevier.com/locate/apsb
www.sciencedirect.com

ORIGINAL ARTICLE

Paeoniflorin alleviates hypobaric hypoxia-triggered lung injury through targeting MEK2 to modulate ERK2−SGK1 signaling

Zhenhui Wu[a,b,†], Yihao Wang[b,*,†], Renjie Wang[b,c,†], Rong Gao[b,d], Shubei Li[b,d], Bodan Tu[b,c], Xiubing Yin[b,d], Maoxing Li[b], Wei Zhou[b], Huanhua Xu[a], Zhenfeng Wu[a], Zengchun Ma[b,d], Xianglin Tang[b], Chengrong Xiao[b], Yue Gao[a,b,c,d,e,*]

[a]*School of Pharmacy, Jiangxi University of Chinese Medicine, Nanchang 330000, China*
[b]*Beijing Institute of Radiation Medicine, Beijing 100850, China*
[c]*School of Chinese Medicine, Tianjin University of Traditional Chinese Medicine, Tianjin 301617, China*
[d]*School of Pharmacy, Guangdong Pharmaceutical University, Guangzhou 510006, China*
[e]*Department of Nephrology, First Medical Center of Chinese PLA General Hospital, Nephrology Institute of the Chinese People's Liberation Army, National Key Laboratory of Kidney Diseases, National Clinical Research Center for Kidney Diseases, Beijing Key Laboratory of Kidney Disease Research, Beijing 100853, China*

Received 12 April 2025; received in revised form 3 December 2025; accepted 16 December 2025

KEY WORDS

Paeoniflorin;
Hypobaric hypoxia;
Lung injury;
Proteomics;
Mitochondrial homeostasis;
MEK2−ERK2−SGK1 axis;
Ferroptosis;
Mitochondrial

Abstract Hypobaric hypoxia-induced lung injury can exacerbate the incidence of plateau pulmonary edema, but relevant pharmacologic measures are relatively limited. Here, we investigate the possible role of paeoniflorin (Pae) in hypobaric hypoxia-induced lung injury. Through *in vivo* and *in vitro* experiments, we observed that Pae significantly ameliorated hypobaric hypoxia-triggered oxidative stress, inflammatory response, mitochondrial dysfunction and ferroptosis. Using limited proteolysis-mass spectrometry (LiP-MS), molecular docking, and molecular dynamics simulations, we identified that Pae directly binds to three amino acid residues (K101, D156, and S198) of the MEK2 protein. Knockdown of MEK2 expression *in vivo* and *in vitro* abrogated the protective effect of Pae. It was also observed that Pae promotes the binding of MEK2 and ERK2 and increases the phosphorylation level of ERK2, leading to its activation. This process induced upregulation of SGK1 and the protective effect of Pae against hypobaric hypoxic

*Corresponding authors.
E-mail addresses: gaoyue@bmi.ac.cn (Yue Gao), hao_1216@126.com (Yihao Wang).
†These authors made equal contributions to the work.
Peer review under the responsibility of Chinese Pharmaceutical Association and Institute of Materia Medica, Chinese Academy of Medical Sciences.

https://doi.org/10.1016/j.apsb.2025.12.024

permeability transition pore

lung injury was dependent on SGK1. Collectively, these findings provide pharmacological evidence that Pae activates SGK1 by targeting MEK2 and mediating MEK2−ERK2 crosstalk, highlighting Pae's potential as a promising therapeutic agent for hypoxic lung injury-related diseases.

1. Introduction

With the rapid advancement of transportation and growing demands in plateau tourism, sports, and military operations, frequent and rapid migration between plains and high-altitude regions has become common. However, the hypobaric, hypoxic environment of high altitudes poses a serious threat to human health. As altitude increases, the respiratory system is the first to be affected by hypoxia, characterized by increased alveolar vascular permeability[1], impaired alveolar fluid clearance[2], and in severe cases, acute hypobaric, hypoxic lung injury and high-altitude pulmonary edema (HAPE) can be triggered, which can endanger life[3,4]. Acute hypoxic lung injury is a severe hypoxic lung disorder responsible for substantial global mortality annually. A key pathologic feature of acute hypobaric hypoxic lung injury is regional alveolar hypoxia[5], which induces lung inflammation[6]. To date, no definitive therapeutic strategies or drugs exist for acute hypoxia-induced lung injury. Thus, elucidating the pathogenesis of acute hypoxic lung injury and developing effective preventive interventions are urgently needed.

Mitochondrial dynamics and homeostasis have recently been identified as the primary mechanism of HAPE[4]. Hypobaric hypoxia-induced lung injury can exacerbate the incidence of plateau pulmonary edema, but relevant pharmacologic measures are relatively limited. In terms of inflammatory regulation, hypoxia drives the accumulation of inflammatory cells in lung tissue, triggering inflammatory cascades[7]. Regarding cell death, hypoxia has been reported to induce apoptosis, necrosis, and ferroptosis in lung tissue cells[8]. In terms of oxidative stress, mitochondrial electron transport chain dysfunction under hypoxia leads to excessive production of reactive oxygen species (ROS), disrupting mitochondrial permeability[9,10]. This disruption further promotes mitochondrial DNA (mtDNA) release, while ROS can also oxidatively modify mtDNA, activating the NLRP3 inflammasome and cGAS−STING pathway-dependent immune responses[11,12]. Drp1-mediated imbalance in mitochondrial dynamics and impaired mitochondrial autophagic flow further exacerbate disturbed cellular energy metabolism[13,14]. In recent years, it has been found that acute hypoxia-induced mitochondrial dysfunction may be the initiator of oxidative damage, inflammatory cascades, cell death and vascular barrier disruption[15,16]. Therefore, targeting oxidative stress induced by mitochondrial homeostatic imbalance is a key strategy for treating hypobaric hypoxic lung injury.

Imbalances in mitochondrial homeostasis, including abnormal mitochondrial membrane potential (MMP), defective mitochondrial biogenesis, impaired mitochondrial dynamics, calcium ion transport, abnormal mitochondrial gene expression, and excessive reactive oxygen species (ROS) production are all directly related to the pathology associated with hypobaric hypoxia lung injury[17,18]. In addition, the generation of these processes further exacerbates mitochondrial dysfunction, leading to a vicious cycle that ultimately triggers hypobaric hypoxic lung injury. MEK2, a core kinase of the MAPK/ERK signaling pathway, regulates cell proliferation, differentiation, and survival by phosphorylating ERK1/2[19]. ERK2 activity is regulated not only by upstream MEK2 signaling but also by SGK1, which enhances ERK signaling activation by promoting MEK/ERK complex formation[20]. MEK2−ERK2 and SGK1 regulate mitochondrial homeostasis through multiple mechanisms. ERK2 promotes mitochondrial division by phosphorylating the mitochondrial division protein DRP1 (Ser616) and modulates mitochondria-dependent apoptosis by regulating BCL-2 family proteins (*e.g.*, BIM, MCL-1)[21]. In contrast, SGK1 reduces mitochondrial permeability transition pore (mPTP) permeability by phosphorylating VDAC1[22] and stabilizes MMP by inhibiting GSK-3β, thereby improving mitochondrial function and mitigating oxidative stress[21]. Furthermore, ERK1/2 and SGK1 synergistically regulate mitophagy, in which activation of ERK1/2 phosphorylation promotes autophagosome formation[23], whereas SGK1 inhibition triggers autophagy-dependent apoptosis through the mTOR-Foxo3a pathway[24]. While previous functional studies of MEK−ERK2 and SGK1 as key regulators of cell survival have focused primarily on oncology, their role in alleviating lung injury by regulating mitochondrial homeostasis to promote cell survival under acute hypoxic conditions remains unreported.

Paeoniflorin (Pae) is a monoterpene glucoside isolated from *Paeonia lactiflora*, a common Chinese medicine that has been used for thousands of years to treat a variety of diseases[25]. Pae combined with luteolin can protect by inhibiting inflammation and oxidative stress in a lipopolysaccharide-induced acute lung injury model[26]. Recent studies have shown that Pae also suppresses oxidative stress and inflammatory responses by restoring MMP, increasing ATP levels and the enzymatic activity of mitochondrial complexes I and III, and inhibiting mitochondrial damage and activation of NLRP3 inflammatory vesicles[27]. Notably, although direct evidence for Pae's efficacy in hypoxic lung injury is limited, its multifaceted roles in counteracting oxidative stress, inflammatory responses, and cell death make it a promising candidate for mitigating hypobaric hypoxic lung injury.

In the present study, we comprehensively evaluated the pharmacodynamic effects of Pae in treating hypobaric hypoxic lung injury using *in vivo* and *in vitro* models. Employing proteomic, genetic, biophysical, and biochemical approaches, we demonstrated that Pae activates ERK2 by targeting three amino acid residues of MEK2, promoting MEK2−ERK2 complex formation. Importantly, Pae's pharmacological effects are dependent on SGK1, and ERK2 activation induces SGK1 upregulation, which in turn alleviates hypobaric hypoxia-induced mitochondrial homeostasis imbalance.

2. Materials and methods

2.1. Animals and treatments

All animal care and experimental procedures were performed in accordance with the Guidelines for the Care and Use of

Laboratory Animals published by the National Institutes of Health (NIH Publication, revised 2011) and approved by the Animal Ethics Committee of the Academy of Military Medical Sciences (No: IACUC-DWZX-2023-P685). Male C57BL/6JGpt mice (20−22 g; 8 weeks) were acquired from Beijing Vital River Laboratory Animal Technology Co., Ltd. (Beijing, China). All mice were housed in ventilated cages under controlled environmental conditions (temperature: 22−23 °C; humidity: 55%−60%) with a standardized 12-h light/dark cycle. Food and water were provided timely throughout the study.

After 3 days of adaptive feeding, the mice were divided evenly into six groups (n = 7/group): (1) Control group (Con); (2) Hypobaric hypoxia model group (Mod); (3) Mod group + Pae (Pae, MCE, NJ, USA, HY-N0293) 12.5 mg/kg (Mod + Pae-L); (4) Mod group + Pae 50 mg/kg (Mod + Pae-H); (5) Mod group + acetazolamide (ACZ, MCE, NJ, USA, HY-B0782) 100 mg/kg (Mod + ACZ). Pae group and ACZ group mice were orally administered once a day for 7 consecutive days. The Con and Mod group mice were orally administered ultrapure water daily for 7 consecutive days. To suppress MEK2 levels, mice were injected with U0126 (3 mg/kg dissolved in sterile saline, MCE, NJ, USA, HY-12031A) for 7 consecutive days. Except for the Con group, all groups were placed inside a chamber under hypobaric hypoxia (Guizhou Fenglei Aviation Ordnance Co., Ltd., China, DWCF50-IIA) continuously for 72 h to ensure food and drinking water, raised to a simulated altitude of 7000 m at a speed of 10 m/s. During hypoxia exposure, administer the drug to mice twice. The experiments for the *in vivo* study are illustrated in Figs. 1B, 9A and 10A. After hypobaric hypoxia exposure, blood was collected from the mouse eye sockets, and serum was extracted from all mice, followed by the removal of lung tissue. Serum samples were separated to determine the levels of oxidative stress and inflammatory indicators. The water content of lung tissue was calculated based on wet and dry weight. Lungs were separated, fixed in 4% paraformaldehyde, and stored at −80 °C separately.

2.2. Cell culture and treatments

The Human Pulmonary Microvascular Endothelial Cells (HPMEC cells) were cultured in Dulbecco's modified Eagle's medium (DMEM, Gibco, MA, USA, 6124092), supplemented with 10% fetal bovine serum (FBS, Gibco, MA, USA, 10099-141) and 1% penicillin/streptomycin at 37 °C in a controlled 5% CO_2 incubator. HPMEC cell lines were purchased from ScienCell™ (CA, USA, Catalog #3000). The cells were passaged at a rate of 1:4 every three days for subsequent experiments. $CoCl_2$ (300 μmol/L, Sigma−Aldrich, STL, USA, 60818) was used to induce an *in vitro* hypoxic microenvironment.

2.3. Enzyme-linked immunosorbent assay (ELISA)

The cytokine levels of TNF-α, IL-1β, IL-6, IL-10, and iNOS in lung tissues, bronchoalveolar lavage fluid (BALF), and HPMEC cells were examined using specific assay kits according to the manufacturer's instructions. The levels of MDA, CAT, SOD, T-SOD, T-AOC, GSH, and GSH-Px in lung tissues and HPMEC cells were quantified using ELISA kits (mmbio, Jiangsu, China). The kits used are listed in Supporting Information Table S1.

2.4. Detection of iron in tissues and cells

The concentrations of iron in lung tissues were measured by Iron Assay Kit (I291, DOJINDO, Japan). In brief, fresh lung tissues were collected and washed with ice-cold PBS, and 100 mg tissue was grinded with liquid nitrogen. Add 100 μL of probe solution to each of the standard and sample wells. The 96-well plates were incubated in an incubator at 37 °C for 1 h. The absorbance at 593 nm was measured. To visualize and quantify the total iron and Fe^{2+} in the cells, a total iron assay kit (Servicebio, Wuhan, China, G4301), and a ferrous ion content assay kit (Solarbio, Beijing, China, BC5415) were used. After washing with PBS, the cells were incubated with FerroOrange (2 μmol/L) probes for 30 min at 37 °C. Then, the cells were observed and captured with laser confocal microscopy (Zeiss, Jena, Germany, LSM880). Similarly, the 96-well plates were incubated in an incubator at 37 °C for 1 h. The absorbance at 593 nm was measured with Cytation™ 5 cell imaging multifunctional microplate detection system (Agilent, CA, USA, BioTek Cytation5).

2.5. Lung index, lung water content and lung tissue wet/dry (W/D) weight ratio

Mice were weighed and recorded before the autopsy, anesthetized by intraperitoneal injection of 0.6% pentobarbital sodium solution (0.1 mL/10 g), fixed in a supine position, the thoracic cavity was opened, and whole lung tissue was removed. After rinsing in precooled saline and adequate absorption of excess water from the surface of the lung tissue by the filter paper, it was placed on tin foil and weighed, and the weight of the lung tissue was recorded as wet weight. The lung tissues were wrapped with tin foil and placed in an oven at a temperature of 60 °C for 72 h. After the weight of the lung tissues was constant, the dry weight was recorded. Lung index, lung water content and wet/dry ratio were calculated according to Eqs. (1)−(3):

$$\text{Lung index (\%)} = \text{Wet weight of whole lung tissue/Mice body weight} \times 100 \quad (1)$$

$$\text{Lung water content (\%)} = (\text{Wet weight} - \text{Dry weight})/\text{Wet weight} \times 100 \quad (2)$$

$$\text{Wet/dry (\%)} = \text{Wet weight/Dry weight} \times 100 \quad (3)$$

2.6. Immunohistochemistry (IHC) of the lung tissue

The lung tissue was fixed with 4% paraformaldehyde, embedded in paraffin, and sectioned. After dewaxing and rehydration, antigen retrieval was performed using either heat-induced epitope retrieval or enzymatic digestion. Endogenous peroxidase activity was blocked with 3% H_2O_2, followed by blocking of nonspecific binding sites with serum. The sections were sequentially incubated with primary antibody (specific target protein antibody, overnight at 4 °C) and secondary antibody. Target signals were visualized using a chromogenic substrate, followed by hematoxylin counterstaining for nuclei. The sections were dehydrated through a graded ethanol series, cleared in xylene, and mounted with neutral balsam for microscopic analysis to localize target protein expression. The antibodies used are listed in Supporting Information Table S2.

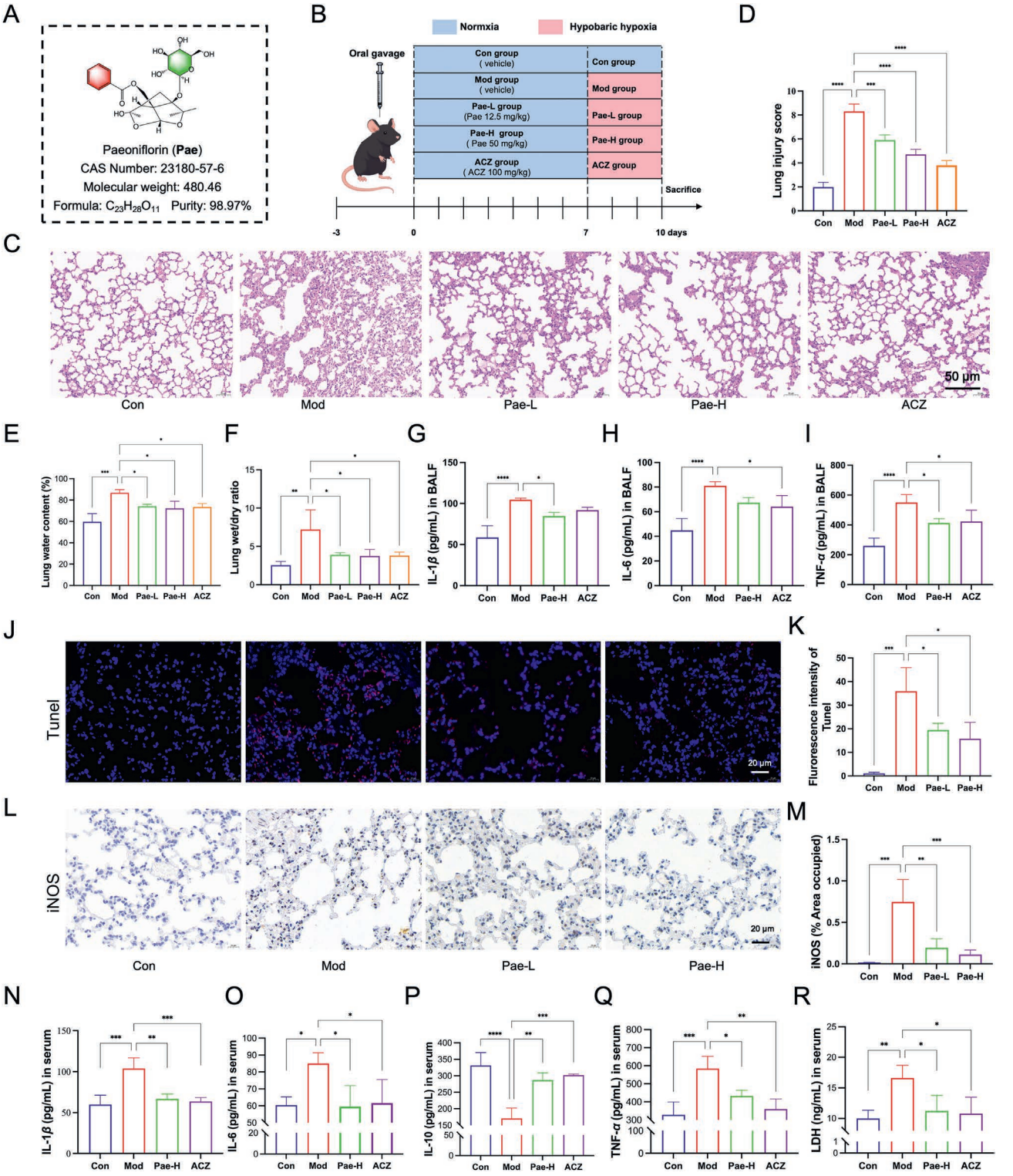

Figure 1 Pae ameliorates hypobaric hypoxia-induced lung injury. (A) Molecular structure information of paeoniflorin (Pae). (B) Schematic diagram of the experimental design in mice. (C) HE pathology of lung tissue in C57 mice ($n = 3$). (D) Lung tissue HE pathology damage score ($n = 3$). (E) C57 mouse lung water content analysis ($n = 3$). (F) C57 mouse lung wet to dry weight ratio analysis ($n = 3$). (G−I) BALF inflammatory factor (IL-1β, IL-6, TNF-α) analysis in C57 mice ($n = 4$). (J, K) Lung tissue TUNEL staining analysis ($n = 3$). (L, M) Immunohistochemical analysis of lung tissue iNOS expression ($n = 3$). (N−Q) ELISA analysis of inflammatory factor (IL-1β, IL-6, IL-10, TNF-α) changes in mouse serum ($n = 4$). (R) Effect of Pae on serum LDH in mice ($n = 4$). P values are calculated by one-way ANOVA followed by the Tukey's test. Data are presented as mean ± SD; $^{*}P < 0.05$; $^{**}P < 0.01$; $^{***}P < 0.001$; $^{****}P < 0.0001$.

2.7. Mitochondrial permeability transition pore (mPTP)

The experiment was performed according to mPTP (Thermo, WLM, USA, M34153) reagent instructions. In brief, take up 50 μL DMSO and dissolve 1 tube of Calcein AM to make a 1 mmol/L Calcein AM master mix. HPMEC cells were trypsin-digested and resuspended in a culture medium and counted to a density of 1×10^6 cells/mL. Take the appropriate amount of cells and centrifuge them at $1000 \times g$ for 5 min, discard the supernatant, and resuspend them by adding the appropriate volume of Calcein AM staining solution, fluorescence quenching work solution. The cells were incubated at 37 °C for 30 min, and after incubation, the cells were collected by centrifugation at $1000 \times g$ for 5 min at room temperature. Cells were resuspended with 400 μL PBS. The samples were then analyzed by flow cytometry, and observed under a laser confocal microscope.

2.8. Detection of intracellular and mitochondrial lipid peroxidation levels

Intracellular and mitochondrial lipid peroxidation were measured with BODIPY™ 581/591 C11 probes (Thermo, WLM, USA, D3861), mitoSOX™ (Thermo, WLM, USA, M36009), and mitoTracker™ green FM (Thermo, WLM, USA, M7514), respectively, using a confocal microscope. HPMEC cells were seeded into confocal dishes and subsequently exposed to mitoSOX™ (5 μmol/L), MitoTracker Green (5 μmol/L), or BODIPY-C11 (5 μmol/L) in the medium with the dyes, which was then placed in an incubator (37 °C with 5% CO_2) for 30 min, respectively. After adding DAPI to the medium for 10 min to label the nuclei, the cells were washed with PBS and detected by laser confocal microscopy (Zeiss, Jena, Germany, LSM880).

2.9. Proteomics LC−MS/MS and data analysis

70 μg protein samples from lung tissues and HPMEC cells were prepared into peptide mixtures for LC−MS/MS analysis (Multi-Protease Strategy Identifies Three PE2 Missing Proteins in Human Testis Tissue, 2017). For limited proteolysise-mass spectrometry (LiP-MS) samples, 100 μg HPMEC whole protein was incubated with 80 μmol/L Pae and ddH_2O respectively, and then enzymatically digested into peptide mixtures with protease K and Trypsin in sequence (A machine learning-based chemoproteomic approach to identify drug targets and binding sites in complex proteomes). All peptide mixtures are cleaned by a home-made C18 column before entering the mass spectrum. Proteomic analysis was performed by Vanquish™ Neo UHPLC coupled an Orbitrap Exploris™ 480 mass spectrometry (Thermo, WLM, USA). The peptide mixture was dissolved in a buffer of 1% FA and 1% ACN, then fed onto a Trap column of 75 μm × 2 cm, and finally entered the mass spectrum eluted by a nonlinear gradient through a 75 μm × 25 cm C18 analytical column. The range of MS survey scan is 350−1200 *m/z*. Normalized AGC target is set to 300% and maximum ion injection time is set to 25 ms. The data dependent acquirement mode is used to collect MS/MS spectrum, and the cycle time of 2 s is controlled, and the ions with the highest abundance in the MS survey scan are fragmented and scanned at a resolution of 15,000. Normalized AGC target is set to 50%, and other parameters are set to default.

Raw data were processed using Proteome Discoverer (v3.0). Lung tissue samples were referred to Swiss-Prot reviewed mouse library, and HPMEC cell samples were referred to Swiss-Prot reviewed human library. It is worth emphasizing that Lip-MS raw data is searched by the semi-enzyme digestion method. Retain the default values for other parameters. Data visualization analysis is mainly based on the R platform, as follows: differentially expressed proteins (DEPs) were screened by the Bioconductor package limma[28]. Proteins with $|\log2 \text{ (fold change)}| > 1$ and P value < 0.05 were identified as DEPs. Functional enrichment analysis of KEGG and GO was performed by the ClusterProfiler package[29]. GSEA analysis was conducted by Bioconductor package enrichplot, and protein interaction network analysis was performed by STRING database (https://cn.string-db.org/) and Cytoscape software.

2.10. Western blot analysis

Protein lysates were extracted using RIPA lysis buffer. Protein extracted from cells or lung tissues was quantified using a BCA protein assay kit (Epizyme, Shanghai, China, ZJ101). Equal amounts of protein from each group (20 μg) were separated *via* SDS-PAGE and transferred to polyvinylidene fluoride (PVDF) membranes (Bio-Rad, CA, USA). After blocking, the blots were probed with primary antibody at 4 °C overnight. The antibodies used are listed in Table S2. This was followed by the incubation with horseradish peroxidase (HRP)-conjugated secondary antibody. Bands were detected using an ECL detection kit and analyzed with ImageJ software.

2.11. Cellular thermal shift assay (CETSA)

HPMEC cells density increased to 60%, drugs were added (Con group and Pae (100 μmol/L) group), followed by incubation at 37 °C in a 5% CO_2 incubator for 1 h. The cells were then washed twice with PBS, and cellular proteins from each group were collected and resuspended in RIPA lysis buffer (containing 150 μL RIPA, 1% protease, and phosphatase inhibitors). The proteins from each group were equally divided into 8 aliquots and transferred to PCR tubes. The PCR thermal cycler was set to 8 temperatures (42, 44, 47, 51, 54, 59, 62, and 66 °C). Each protein aliquot from all groups was heated at the designated temperature for 3 min, followed by equilibration at room temperature for 3 min. Subsequently, all samples were flash-frozen in liquid nitrogen, and cell lysis was performed through three cycles of freezing and thawing. After vortex mixing, the samples were centrifuged to collect the supernatant. The supernatant was mixed with 5 × loading buffer and boiled at 100 °C for 10 min. The final samples were subjected to Western Blot analysis.

2.12. Drug affinity responsive target stability (DARTS)

HPMEC density increased to 60%, drugs were added (Con group and Pae (10, 20,100 μmol/L) group) and incubated in 5% CO_2 incubator for 1 h at 37 °C. Cells were subsequently washed twice with PBS, cellular proteins of each group were collected, unstably bound protein was added to proteinase K, then RIPA lysate (containing 150 μL RIPA, 1% protease, and phosphatase inhibitors) was added, 100 °C was boiled for 10 min. The final sample was used for Western Blot detection.

2.13. Microscale thermophoresis (MST) assay

First, MEK2 protein was labeled with NHS dye. Different concentrations of Pae were added to the buffer containing the labeled

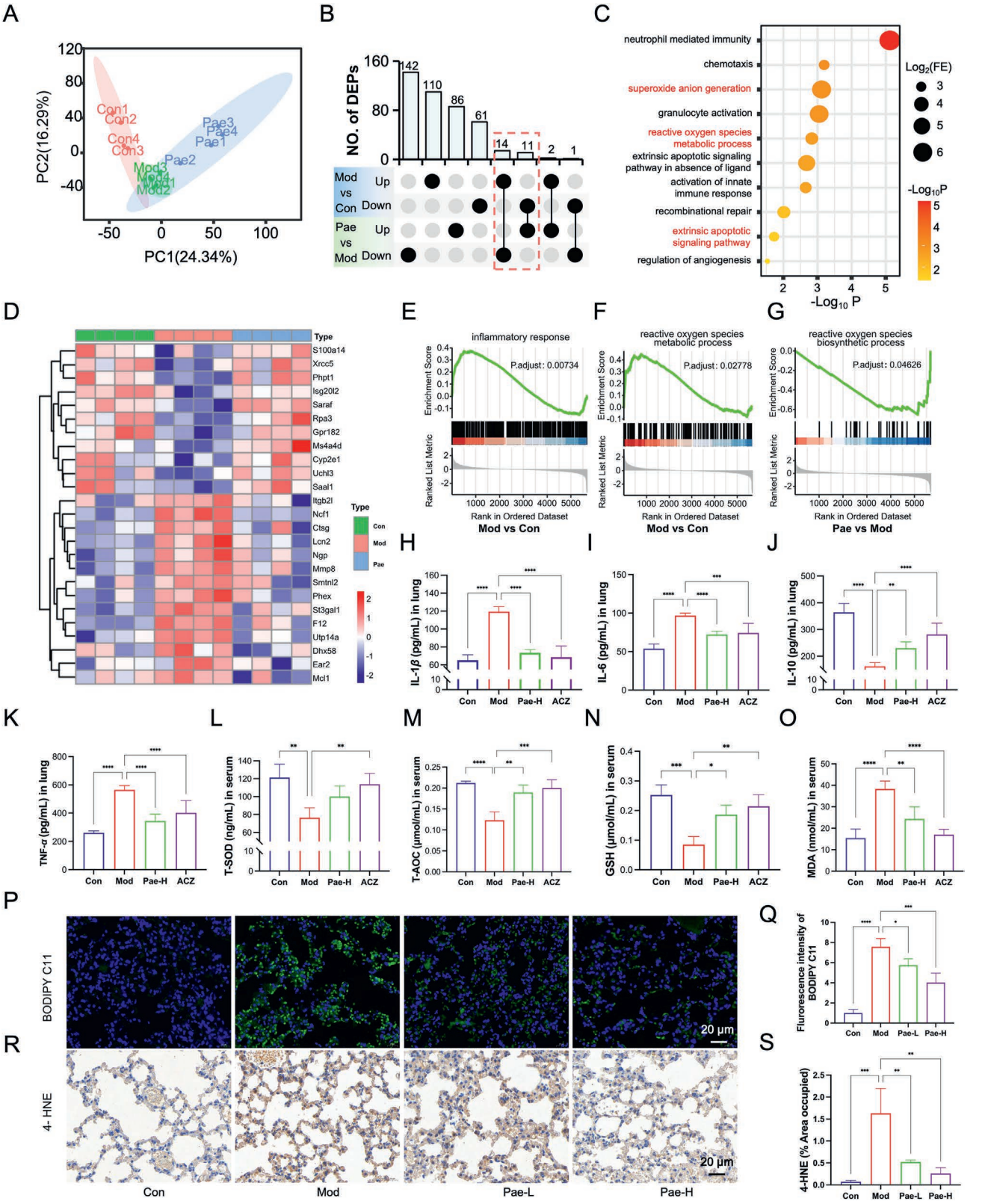

Figure 2 Proteomics reveals that Pae inhibits hypobaric hypoxia-induced reactive oxygen species generation and inflammatory response in lung tissue. (A) PCA analysis ($n = 4$). (B) Classification of differential proteins. (C) KEGG functional enrichment analysis of reversed proteins. (D) Heat map analysis of reverse differential proteins. (E, F) GSEA analysis between Mod and Con groups. (G) GSEA analysis between Pae and Mod groups. (H−K) ELISA analysis of changes in the levels of inflammatory factors (IL-1β, IL-6, IL-10, TNF-α) in lung tissues of C57 mice ($n = 6$). (L−O) ELISA analysis of changes in the levels of serum oxidative stress indicators (T-SOD, T-AOC, GSH, MDA) in C57 mice ($n = 6$). (P, Q) BODIPY C11 staining analysis of changes in lipid peroxidation in lung tissue of C57 mice ($n = 3$). (R, S) Immunohistochemical analysis

MEK2 protein and incubated at room temperature for 30 min. Secondly, desalting is performed after protein labeling. Finally, the constant affinity (K_D) constant was analyzed using the Monolith NT.115 software (MicroScale Thermophoresis, Munich, Germany).

2.14. Surface plasmon resonance (SPR) assay

First, after activating the CM5 chip, fix the MEK2 protein to the CM5 chip. Secondly, ethanolamine was used to seal the chip for 420 s. Then, different concentrations of Pae were loaded, and the sensor signal was analyzed based on changes in reflected light intensity over time. Finally, the constant affinity (K_D) constant, was calculated using BiacoreX100 software (Cytiva, MA, USA).

2.15. Cell transfection

The human *MAP2K2* gene (*MEK2*) siRNA for this experiment was ordered from Shanghai Hanbio (Shanghai, China). The corresponding target sequences are listed as followed: F: 5-GCAACUCGCCGUACAUCGUGG-3; R: ACGAUGUACG GCGAGUUGCAU (si-MEK2). The experiment was divided into five groups: si-NC, si-NC + Mod, si-NC + Mod + Pae, si-MEK2+Mod, and si-MEK2+Mod + Pae, with three replicates in each group. Two 1.5 mL EP tubes were prepared for each well, labeled as tube A and tube B, respectively, and placed on a rack for subsequent use. Tube A: 5 μL of 20 μmol/L si-RNA was added to 100 μL of separate DMEM medium. Tube B: 5 μL of RNAFit was added to 100 μL of separate DMEM medium. Then all the liquid in tube B was transferred to tube A, mixed well, and left for 20 min to form the transfection complex. The effect of siRNA silencing was detected by Q-PCR and Western blot assay 48 h after transfection.

2.16. Establishment of stable cell lines

Lentivirus target *MAP2K2* (*MEK2*) and (human source) (*MAP2K2*) was selected for this experiment from Genechem (Shanghai, China). The vector used was numbered GV492, with the sequence of components Ubc-MCS-3FLAG-CBh-gcGFP-IRES-puromycin. Briefly, HPMEC cells in good condition were selected and inoculated in 12-well plates, which were divided into 4 groups: group Con (control group, containing only complete medium), group M (control virus-infected group containing only complete medium), group A (lentivirus + HiTransG A), and group P (lentivirus + HiTransG P). Lentiviral titers were diluted in three gradients: MOI 10, MOI 50, and MOI 100. Corresponding lentiviruses were diluted in serum-containing complete DMEM medium in three titers (1×10^7 TU/mL, 5×10^7 TU/mL, and 1×10^8 TU/mL). The original culture in the 12-well plate was aspirated and virus was added for infection. The HPMEC cells were screened by puromycin (2 μg/mL) for 7 days.

2.17. Immunoprecipitation (IP) assay

Protein interactions were identified using a Pierce Crosslink Immunoprecipitation Kit (Thermo, WLM, USA, 26146). Briefly, the MEK2 antibodies were covalently crosslinked onto Protein A/G resin with the incubation of disuccinimidyl suberate for 1.5 h. Cell lysates prepared with IP Wash Buffer were then incubated with the resin overnight at 4 °C. Finally, the immunoprecipitated proteins were analyzed by Western blotting.

2.18. Construction of the MEK2-mut expression plasmid and MEK2-mut protein purification

The cDNA of the human *MEK2*-Mut (101K, 156D, and 198S both mutated to Ala) protein was cloned using RTPCR and inserted into the pET28a vector with N segment carries a 6 × His tag as well as a thrombin cleavage site. The plasmid containing *MEK2*-Mut cDNA was transformed into *Escherichia coli* (BL21-CodonPlus (DE3)-RIPL), and clones with the target gene were selected using agar plates containing chloramphenicol. The *E. coli* containing the recombinant plasmid was precultured overnight in 4 mL of autoclaved Luria−Bertani (LB) medium at 37 °C with shaking at 200 rpm. The seed culture was inoculated at a rate of 1%−2% into 50 mL of LB medium and cultured at 37 °C with shaking at 150 rpm for 4 h. Next, 1 mmol/L isopropyl thio-β-D-galactoside (IPTG) was added to initiate the expression of the target genes, and continue shaking at 37 °C, 120 rpm for 4 h. The recombinant MEK2-Mut was then purified from intracellular proteins using sonication and Ni-affinity chromatography. After SDS−PAGE analysis and verification, the eluent was dialyzed and concentrated to obtain high-purity MEK2-Mut protein.

2.19. AAV transduction

To perform lung tissue vascular endothelial cells-selective gene knockdown *in vivo*, an endothelial cells-specific gene transduction system was employed using an AAV-mediated gene delivery system (recombinant AAV-VEC), under the control of an endothelial cells-selective Tie1 promoter (HanBio Co., Ltd., Shanghai, China)[30-32]. For lung tissue vascular endothelial cells-selective MEK2 knockdown, AAV-VEC-Tie1-EGFP-mir30-shMEK2 particles with Tie1 promoter were generated by co-transfecting plasmids, including shuttle plasmid (carrying the *MEK2* shRNA), the pAAV-RC plasmid coding for AAV capsids and pHelper plasmid, into 293T cells with Lipofiter transfection reagents (HanBio Co., Ltd., Shanghai, China). AAV-VEC was injected into the respiratory tract of mice by modified intranasal method[33]. Briefly, male C57BL/6J mice were anesthetized with isoflurane in a small animal anesthesia machine (VMR-Matrx VIP3000, MIDMARK, OH, USA). The first person restrains the mouse head up at a 45 °C angle with the right hand and gently pinched shut mouth with the left hand. A second person delivered a total volume of 80 μL AAVs (virus titer $>1.2 \times 10^{12}$ vg/mL) into the nasal cavity of mice in two drops (40 μL each). The droplets were made to be inhaled passively. Intervention treatment started four weeks after titration of AAV-VEC.

2.20. Statistical analysis

All statistical analyses were performed using GraphPad Prism 10 (GraphPad software, CA, USA). Data are presented as mean ± standard deviation (SD) of at least three independent experiments. Differences between multiple groups were analyzed by one-way ANOVA followed by Tukey's test; pairwise

of 4-HNE expression in lung tissue of C57 mice ($n = 3$). P values are calculated by one-way ANOVA followed by the Tukey's test. Data are presented as mean ± SD; *$P < 0.05$; **$P < 0.01$; ***$P < 0.001$; ****$P < 0.0001$.

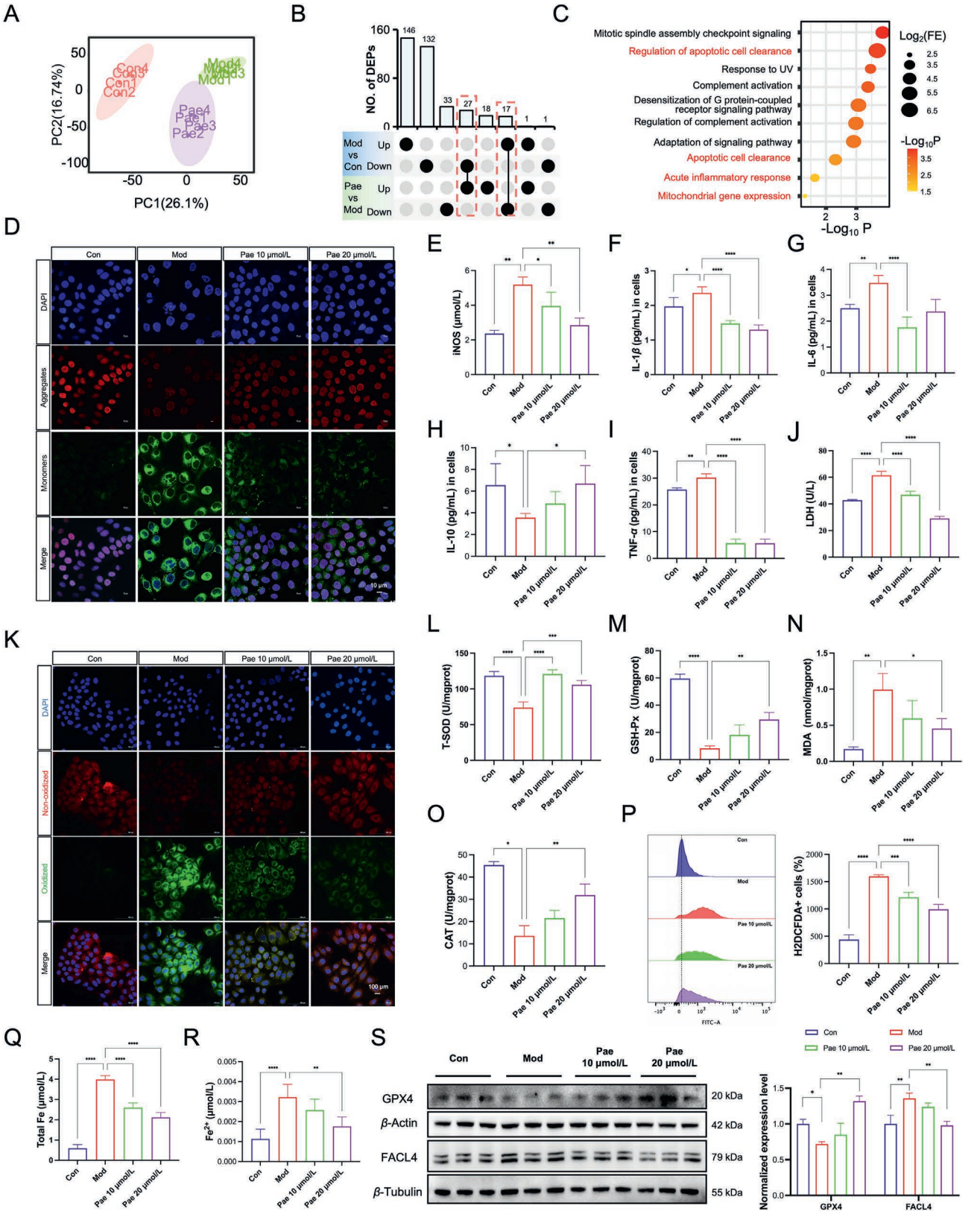

Figure 3 Pae inhibits hypoxia-induced oxidative stress, inflammatory response, and ferroptosis *in vitro*. (A) PCA analysis ($n = 4$). (B) Differential protein classification. (C) KEGG functional enrichment analysis of reversed proteins. (D) Confocal microscopy analysis of JC-1 levels in HPMEC cells ($n = 3$). (E) ELISA analysis of intracellular iNOS levels ($n = 4$). (F−I) ELISA analysis of changes in intracellular levels of inflammatory factors (IL-1β, IL-6, IL-10, TNF-α) ($n = 4$). (J) Effect of Pae on Intracellular LDH level ($n = 4$). (K) BODIPY C11 staining analysis of cellular lipid peroxidation changes ($n = 3$). (L−O) ELISA analysis of changes in intracellular levels of oxidative stress indicators

comparisons were performed using Dunnett's method in ANOVA. $P < 0.05$ was considered statistically significant.

3. Results

3.1. Pae ameliorates hypobaric hypoxia-induced lung injury

The molecular structure of Pae is shown in Fig. 1A. To investigate the pulmonary protective effect of Pae *in vivo*, we established a mouse model of hypobaric hypoxic lung injury using a hypobaric oxygen chamber to simulate exposure stimulation at 7000 m altitude for 3 days (Fig. 1B). HE staining showed that the mod mice developed severe inflammatory cell infiltration and alveolar wall thickening, whereas the Pae-treated group exhibited a significant inflammation-reducing effect (Fig. 1C and D). In addition, hypobaric hypoxic stimulation caused significant pulmonary edema, whereas acetazolamide and Pae treatment resulted in a significant improvement in lung water content (Fig. 1E) and wet-to-dry weight ratio (Fig. 1F). Further, ELISA results showed that hypobaric hypoxia increased pro-inflammatory cytokine levels (IL-1β, IL-6, TNF-α) in BALF, and that Pae intervention was able to reverse this change (Fig. 1G−I). Notably, Tunel staining showed that Pae was able to ameliorate DNA damage in lung tissues induced by hypobaric hypoxia (Fig. 1J and K), suggesting a protective effect against apoptosis. Immunohistochemical results further revealed that the upregulation of iNOS in lung tissues was effectively suppressed after Pae intervention (Fig. 1L and M). In addition, hypobaric hypoxia significantly up-regulated serum pro-inflammatory factor (IL-1β, IL-6, TNF-α) levels (Fig. 1N−Q) and LDH levels and down-regulated anti-inflammatory factor (IL-10) levels (Fig. 1P) in mice. Pae reversed serum inflammatory factor and LDH levels (Fig. 1R). Taken together, our data suggest that Pae ameliorates hypobaric hypoxia-induced lung injury.

3.2. Proteomics reveals that Pae inhibits hypobaric hypoxia-induced reactive oxygen species generation and inflammatory response in lung tissue

To elucidate the mechanism underlying Pae's protective effects, a lung tissue proteomic analysis was performed. We obtained high-quality proteomics data (Supporting Information Fig. S1A and S1B). Further analysis revealed that Pae was able to significantly reverse the proteomic profile of the mod group on the second principal component (Fig. 2A). Through differential protein screening (Fig. S1C and S1D) and integration comparison, we found 25 DEPs that could be reversed by Pae (Fig. 2B). KEGG analysis revealed that these DEPs were mainly enriched in inflammatory response, reactive oxygen species metabolism, and apoptosis pathways (Fig. 2C). Specifically, inflammatory signaling proteins (NCF1, MMP8), reactive oxygen species homeostasis regulators (NCF1, LCN2), and apoptosis-related proteins (MCL1) were significantly overexpressed in the Mod group, whereas Pae treatment was able to effectively reverse the expression levels of these proteins (Fig. 2D). Additionally, gene set enrichment analysis (GSEA) also revealed the important roles of inflammatory response and reactive oxygen species metabolic pathways in the pharmacological activity of Pae (Fig. 2E−G). This finding is highly consistent with the results of enrichment network analysis of differential proteins (Fig. S1E and S1F). At the level of experimental validation, the trend of inflammatory factor content in lung tissue was highly consistent with the proteomic data (Fig. 2H−K). Meanwhile, ELISA results showed that Pae significantly reversed this change of T-SOD, T-AOC, GSH, and MDA induced by hypobaric hypoxia in serum (Fig. 2L−O). This conclusion was further supported by the results of BODIPY C11 staining (Fig. 2P and Q) and 4-HNE immunohistochemistry (Fig. 2R and S) in lung tissues. This reveals that Pae inhibits hypobaric hypoxia-induced reactive oxygen species generation and inflammatory response *in vivo*.

3.3. Pae inhibits hypoxia-induced oxidative stress, inflammatory response, and inhibits ferroptosis

To further evaluate the *in vitro* anti-hypoxic effect of Pae and its protective effect against lung injury, we chose cobalt chloride ($CoCl_2$) to stimulate human pulmonary microvascular endothelial cells (HPMEC) in order to establish the *in vitro* hypoxic injury[34]. CCK-8 results revealed that 300 μmol/L $CoCl_2$ significantly inhibited HPMEC cell proliferation, and 10 and 20 μmol/L Pae significantly reversed the effect of $CoCl_2$ (Supporting Information Fig. S2A). Pae was found to increase the viability of HPMEC cells by Calcein-AM staining (Fig. S2B). We further carried out a proteomic analysis of HPMEC cells. A total of 5482 proteins were identified in the control (Con), model (Mod), and Pae intervention groups (Fig. S2C). PCA results showed that Pae was able to reverse the proteomic profile of the mod group (Fig. 3A). Similarly, by differential protein screening (Fig. S2D and S2E) and integration comparison, we screened 44 DEPs that could be reversed by Pae (Fig. 3B). Functional enrichment analysis of these DEPs resulted in re-emphasizing pathways such as apoptotic cell clearance, inflammatory response, and mitochondrial gene expression (Fig. 3C). At the level of cellular experimental validation, we first examined the levels of MMP, apoptosis, and ROS. The decrease in MMP also suggests the onset of early apoptosis. The MMP level in the Pae group was significantly enhanced (Fig. 3D, Fig. S2G and S2H). The levels of iNOS and intracellular NO was significantly decreased by Pae intervention (Fig. 3E, Fig. S2F). Annexin V and PI double staining results also confirmed that Pae can significantly alleviate hypoxia-induced apoptosis (Fig. S2I and S2J). Meanwhile, Tunel staining revealed that Pae significantly inhibited $CoCl_2$-induced apoptosis (Fig. S2K).

In addition, Pae significantly reversed the levels of IL-1β, IL-6, IL-10, and TNF-α induced by $CoCl_2$ (Fig. 3F−I). The content of LDH was significantly decreased by Pae intervention (Fig. 3J). In response to oxidative stress, BODIPY C11 staining showed that Pae significantly reduced lipid peroxidation levels in HPMEC cells (Fig. 3K). Correspondingly, we observed that Pae significantly reversed the levels of T-SOD, GSH-Px, MDA, and CAT (Fig. 3L−O). We also found that Pae can significantly alleviate ROS content in HPMEC cells (Fig. 3P, Fig. S2L and S2M). Meanwhile, we also found that Pae significantly reversed the levels of total Fe, Fe^{3+} and Fe^{2+} ions *in vivo* and *in vitro* (Fig. 3Q

(T-SOD, GSH-Px, MDA, CAT) ($n = 4$). (P) Flow cytometry analysis of cellular ROS levels ($n = 3$−4). (Q, R) Effect of Pae on intracellular total Fe and Fe^{2+} levels ($n = 3$−4). (S) Western blot analysis of GPX4 and FACL4 protein levels ($n = 3$). *P* values are calculated by one-way ANOVA followed by the Tukey's test. Data are presented as mean ± SD; *$P < 0.05$; **$P < 0.01$; ***$P < 0.001$; ****$P < 0.0001$.

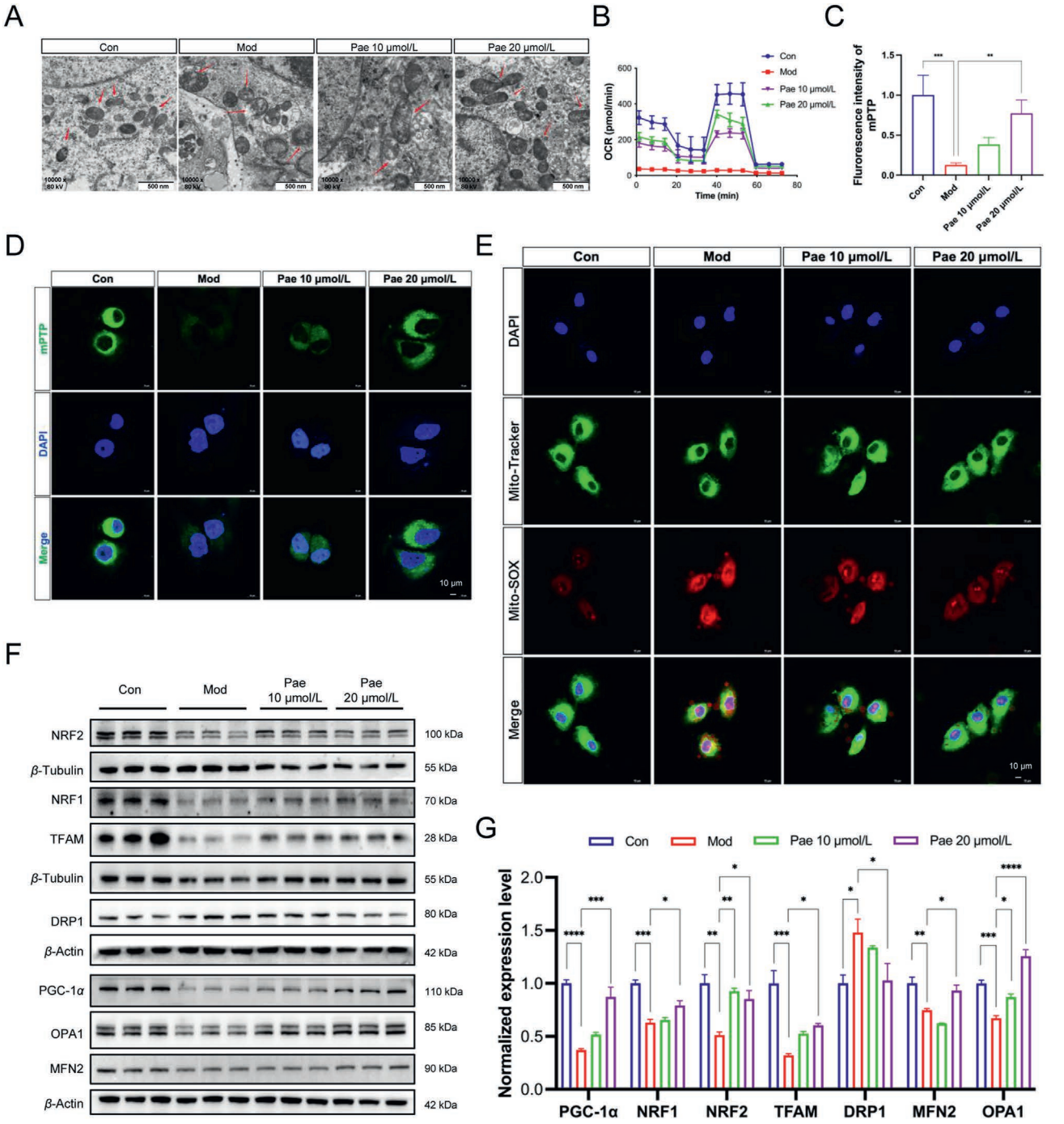

Figure 4 Pae improves mitochondrial function and inhibits hypoxia-induced structural damage and dysfunction of mitochondria *in vitro*. (A) Transmission electron microscopy analysis of changes in cell mitochondrial structure ($n = 3$). (B) Seahorse analysis of OCR Respiration rate ($n = 4–6$). (C, D) Confocal microscopy analysis of mitochondrial permeability transition pore (mPTP) ($n = 3$). (E) Confocal microscopy analysis of mito-SOX mitochondrial activity ($n = 3$). (F, G) Western blot analysis of mitochondrial biogenesis and mitochondrial dynamics-related proteins ($n = 3$). *P* values are calculated by one-way ANOVA followed by the Tukey's test. Data are presented as mean ± SD; $^{*}P < 0.05$; $^{**}P < 0.01$; $^{***}P < 0.001$; $^{****}P < 0.0001$.

and R, Supporting Information Fig. S3A and S3C). Importantly, ROS overproduction and lipid peroxidation are inevitable events triggered by ferroptosis. To further support this finding, Western blot, immunofluorescence, and immunohistochemistry were used to examine the level of GPX4, FACL4 protein, respectively (Fig. 3S, Fig. S3D and S3I. These results further support the finding that Pae improves hypobaric hypoxia-induced lung injury by suppressing oxidative stress and ferroptosis.

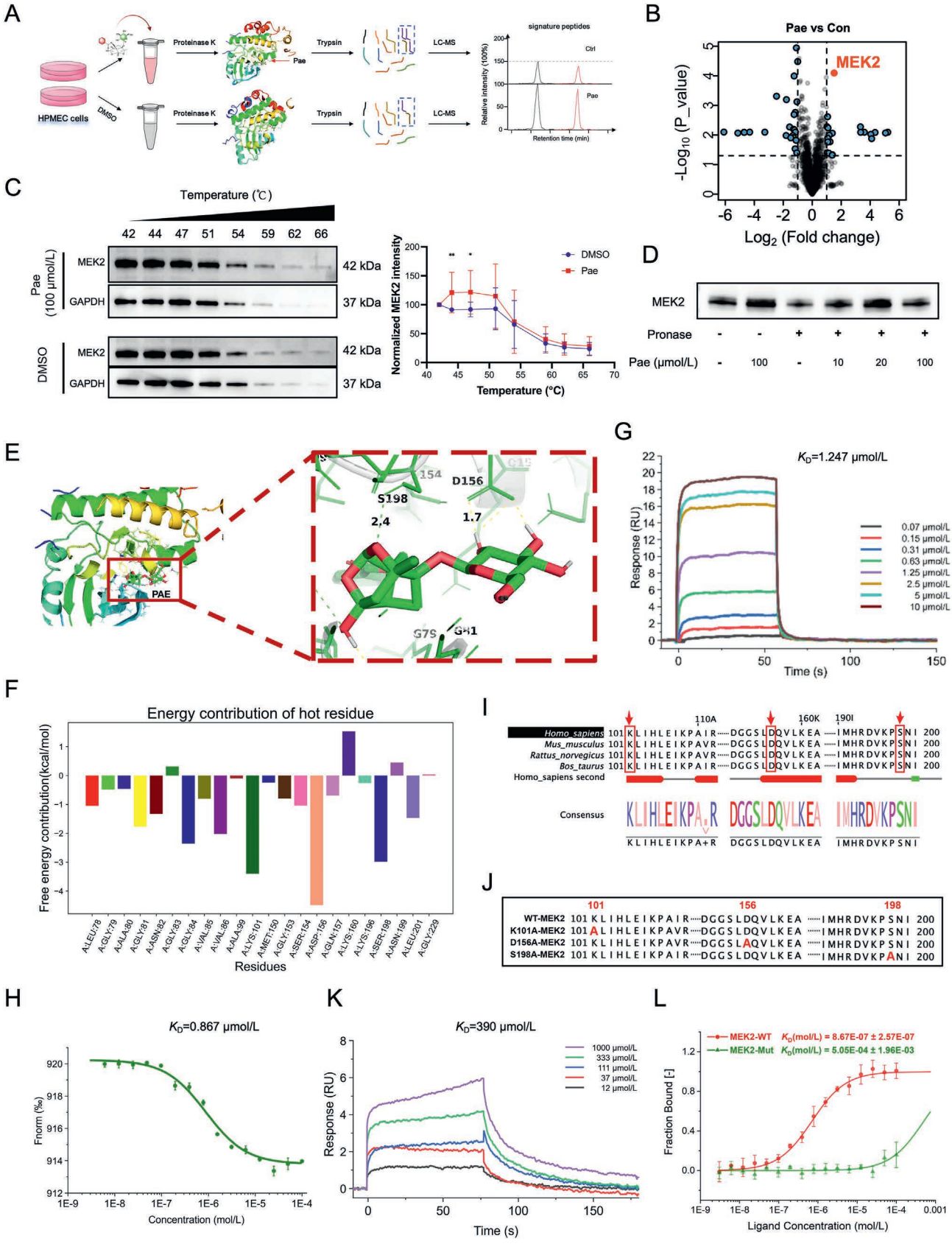

Figure 5 Chemical proteome reveals MEK2 protein as a target of Pae. (A) Schematic diagram of the limited proteolysis-mass spectrometry (LiP-MS) experimental flow. (B) Differential protein volcano plot analysis. (C) Cellular Thermal Shift Assay (CETSA) analysis of Pae and MEK2 protein binding level. (D) Drug Affinity Responsive Target Stability (DARTS) analysis of Pae and MEK2 protein binding levels. (E) 3D

3.4. Pae improves mitochondrial function and inhibits hypoxia-induced structural damage and dysfunction of cellular mitochondria

Apoptosis, ROS production, and ferroptosis are closely associated with mitochondrial function, and mitochondrial homeostasis is critical for iron metabolism, apoptosis resistance, and hypoxic adaptation[35]. Acute hypoxia resulted in reduced mitochondrial number, membrane rupture and ridge breakage, while Pae treatment significantly alleviated this structural abnormality (Fig. 4A). Of interest, this structural improvement is closely related to functional recovery. Pae was found to elevate OCR and mitochondrial respiration rate in a dose-dependent manner by seahorse assay (Fig. 4B). Further analysis of key indicators of mitochondrial function revealed that the mitochondrial mPTP fluorescence intensity was significantly reduced in hypoxia group (Fig. 4C and D), while the mitochondrial superoxide level was significantly increased (Fig. 4E). In contrast, Pae intervention reversed the above changes triggered by hypoxia exposure. The regulation of mitochondrial homeostasis by hypoxia is dual: on the one hand, it contributes to the fragmentation of the mitochondrial network through activation of the splitting protein DRP1 and inhibition of the expression of the fusion protein MFN2/OPA1[36], a dynamic change that may enhance hypoxic adaptation by increasing membrane surface area. On the other hand, however, excessive fragmentation leads to loss of membrane potential and activation of mitochondrial autophagy, creating a vicious cycle[13]. In the present study, Pae can effectively alleviate hypoxia-induced mitochondrial fission/fusion imbalance by regulating the expression levels of proteins such as DRP1, MFN2, OPA1, and PGC-1α (Fig. 4F and G). Combined with previous findings that Pae improves MMP and mPTP function, these results indicate that mitochondrial homeostasis regulation is a key mechanism underlying Pae's pharmacological activity against hypoxic lung injury.

3.5. Chemical proteome reveals MEK2 protein as a target of Pae action

To elucidate the key molecular mechanisms Pae's action, LiP-MS was used to screen potential target proteins (Fig. 5A). PCA showed significant differences in proteomic profiles after Pae treatment (Supporting Information Fig. S4A). The data quality of target screening was good, and the average CV values of both groups of samples were within 20% (Fig. S4B). Volcano maps show significantly more MEK2 in the Pae group (Fig. 5B) and its peptides had good identification quality (Fig. S4C). To confirm MEK2 as a direct target of Pae, CETSA, DARTS, molecular docking, molecular dynamics simulations (MDS), SPR, and MST assays were performed. The results of CETSA and DARTS indicated that Pae could alleviate the thermal degradation of MEK2 (Fig. 5C), and pronase-mediated nonspecific degradation (Fig. 5D). Molecular docking results also revealed that Pae binds stably to MEK2 protein with a binding energy of −8.12 kcal/mol (Fig. S4D and S4E). And the D156 and S198 sites are the closest to Pae, with spatial distances of 1.7 Å and 2.4 Å between them, respectively (Fig. 5E). Subsequently, further analysis by MDS revealed that the RMSD value between MEK2 and Pae was relatively large during the first 18 ns of simulation; it gradually leveled off after 20 ns and maintained in a small range (Fig. S4F). The lowest RMSF values were found in amino acid site 101, 156, and 198, etc (Fig. S4G). The amino acid sites with the highest energy contribution values were found to be the site K101, D156, and S198, according to the ordering of the free energy contribution values. These three sites are Lys101, Asp156, Ser198 (Fig. 5F). The closest amino acid distances after Pae binding to MEK2 were found to be D156, K101, and S198, respectively, as analyzed by spatial structure trajectory changes in MDS (Fig. S4H). The complex energy of Pae binding to MEK2 was calculated and the total free energy of binding was −56.74 kcal/mol (Fig. S4I). The SPR results showed that the KD binding constant of Pae and MEK2 was 1.247 μmol/L (Fig. 5G), and the MST results showed that the KD binding constant of the two was 0.867 μmol/L (Fig. 5H), suggesting that the two have a strong mutual binding effect.

To verify the accuracy of the binding site of Pae and MEK2 protein, we first compared the MEK2 protein homologous among Homo, Mus, Rattus, and Bos species (Fig. 5I). Subsequently, we mutated three sites (K101, D156, and S198) into Ala (Fig. 5J), and predicted the structures of the three-point mutant proteins and the three sites simultaneously mutated proteins (K101A, D156A, S198A, and Mut-3A) by Alphafold3, respectively. Molecular docking showed that the binding energies of Pae to K101A, D156A, S198A, and Mut-3A proteins were −7.34 kcal/mol, −7.23 kcal/mol, −7.19 kcal/mol, and −6.89 kcal/mol, respectively (Fig. S4J). Analysis of the number of hydrogen bonds after binding revealed that the number of HBonds was reduced in K101A-Pae, D156A-Pae, and S198A-Pae compared to MEK2-Pae (Fig. S4K). RMSD was larger after mutation at all three loci compared to MEK2-Pae; K101A, D156A, and S198A were all above MEK2-Pae (Fig. S4L). It is suggested that the binding of Pae to MEK2 is affected and the stability is reduced after the three site mutations. Finally, the KD binding constants of Pae to the point mutated purified protein MEK2 ($MEK2^{Mut}$) were found to be 390 μmol/L (Fig. 5K) and 505 μmol/L (Fig. 5L) as verified by SPR and MST experiments, respectively. Collectively, these data demonstrate that MEK2 is a direct target of Pae, with binding residues at K101, D156, and S198.

3.6. Inhibition of MEK2 causes mitochondrial damage, promotes mPTP opening, and exacerbates lipid peroxidation and ferroptosis in vitro

To verify whether Pae's protective effects against acute hypoxic lung injury are MEK2-dependent, Pae was combined with the specific MEK2 inhibitor U0126. Microscopic observation showed that U0126 aggravated hypoxia-induced cellular shrinkage and apoptotic body formation (Fig. 6A). Flow cytometry results showed that U0126 significantly suppressed Pae-induced MMP

visualization of molecular docking analysis of Pae binding to MEK2 protein. (F) MDS analysis of the amino acid free energy contribution of Pae binding to MEK2 protein. (G) Surface plasmon resonance (SPR) analysis of Pae with MEK2 protein binding level. (H) Microscale Thermophoresis (MST) analysis of Pae with MEK2 protein binding level. (I) Amino acid sequence display of MEK2 protein among different species. (J) Sequence display of three site mutations in Pae binding to MEK2 protein. (K) SPR analysis of Pae binding to MEK2-Mut protein. (L) MST analysis of Pae binding to MEK2 and MEK2-Mut proteins. Dunnett's method in ANOVA test (C) was used for statistical analysis. $*P < 0.05$; $**P < 0.01$.

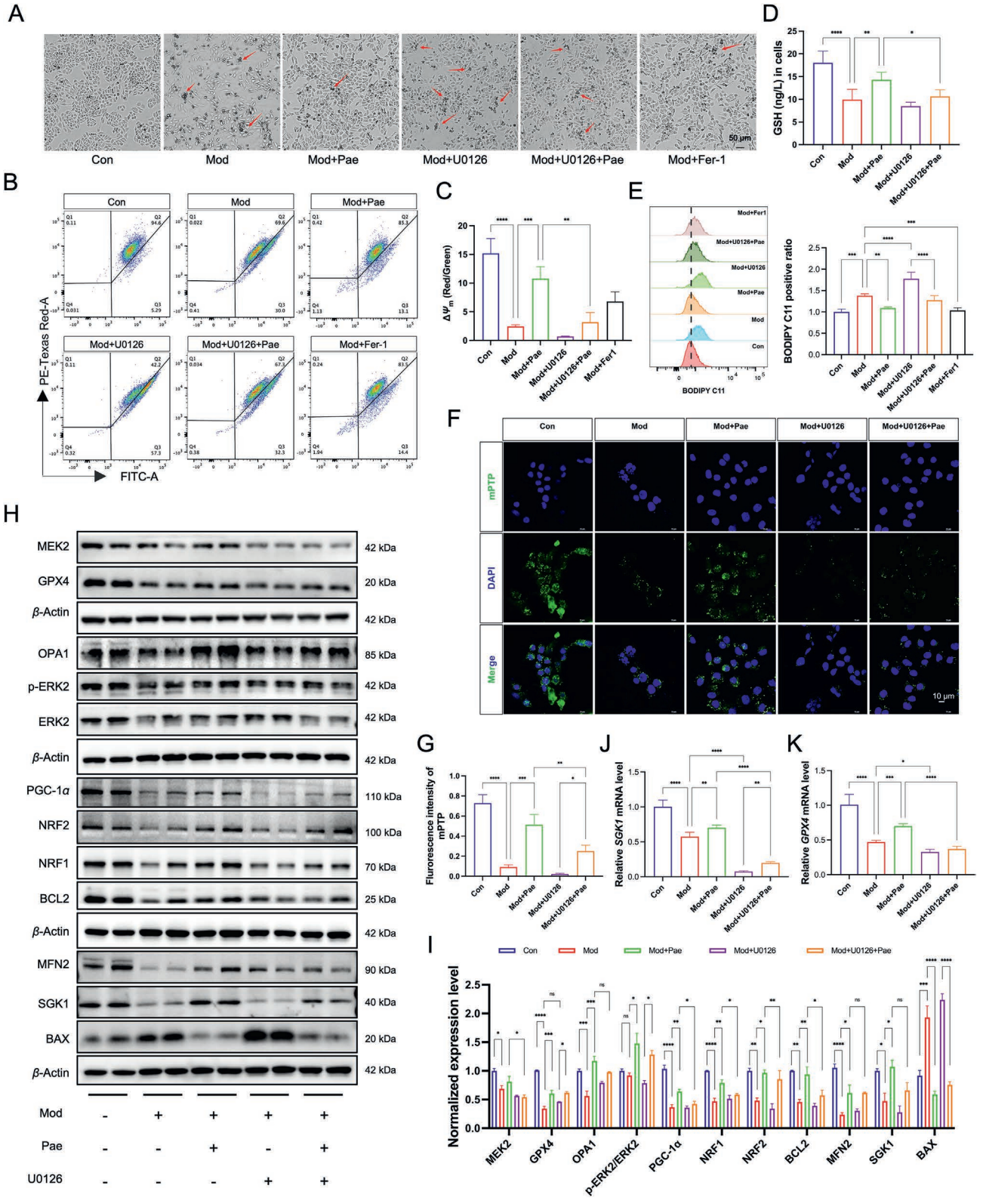

Figure 6 U0126 causes mitochondrial damage, mPTP opening, lipid peroxidation, and ferroptosis *in vitro*. (A) Cell morphology observation ($n = 3$). (B, C) Flow cytometry analysis of cellular MMP ($n = 3$−4). (D) Elisa analysis of cellular GSH levels ($n = 4$−6). (E) Flow cytometry analysis of cellular BODIPY C11 ($n = 3$−4). (F, G) Confocal microscopy analysis of mPTP ($n = 3$). (H, I) Western blot analysis of cellular MEK2, GPX4, OPA1, p-ERK2, ERK2, PGC-1α, NRF2, NRF1, BCL2, MFN2, SGK1, and BAX protein expression changes ($n = 3$−4). (J) Q-PCR analysis of *SGK1* mRNA in HPMEC cells ($n = 4$). (K) Q-PCR analysis of *GPX4* mRNA in HPMEC cells ($n = 4$). *P* values are calculated by one-way ANOVA followed by the Tukey's test. Data are presented as mean ± SD; $^{*}P < 0.05$; $^{**}P < 0.01$; $^{***}P < 0.001$; $^{****}P < 0.0001$; ns: not significant.

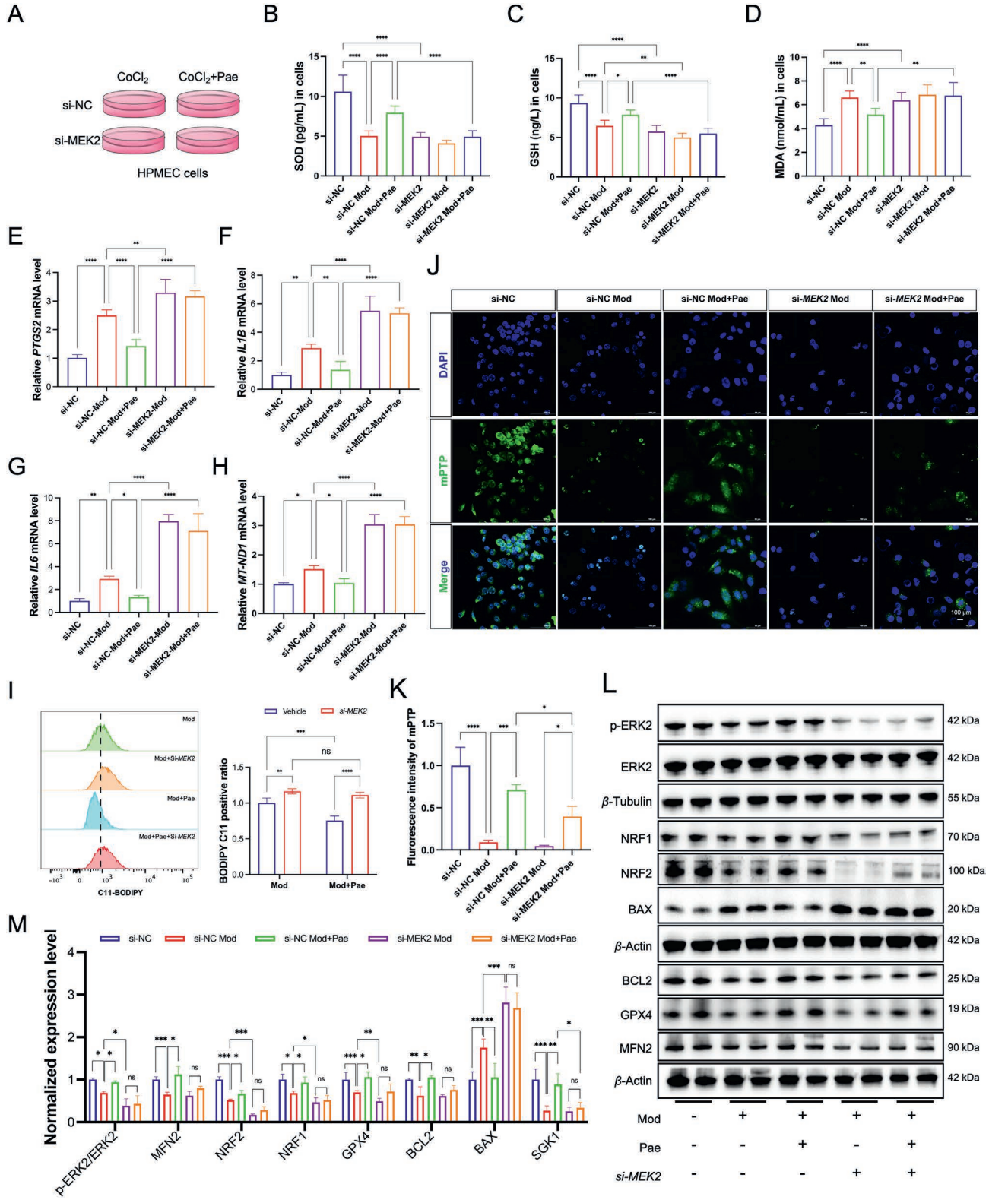

Figure 7 Knockdown of MEK2 in HPMEC cells causes mitochondrial damage, induces mPTP opening and aggravates lipid peroxidation. (A) Schematic diagram of MEK2 knockdown cell experiment. (B−D) ELISA analysis of cellular oxidative stress indicators (SOD, GSH, MDA) levels ($n = 4$). (E−H) Q-PCR analysis of intracellular *PTGS2* (E), *IL1B* (F), *IL6* (G), and *MT-ND1* (H) mRNA levels ($n = 4$). (I) Flow cytometry analysis of cellular BODIPY C11 ($n = 3$−4). (J, K): Confocal microscopy analysis of cellular mPTP changes ($n = 3$). (L, M): Western blot analysis of cellular p-ERK2, ERK2, NRF1, NRF2, BAX, BCL2, GPX4, and MFN2 protein expression ($n = 3$−4). *P* values are calculated by one-way ANOVA followed by the Tukey's test; pairwise comparisons were performed using Dunnett's method in ANOVA. Data are presented as mean ± SD; $^{*}P < 0.05$; $^{**}P < 0.01$; $^{***}P < 0.001$; $^{****}P < 0.0001$; ns: not significant.

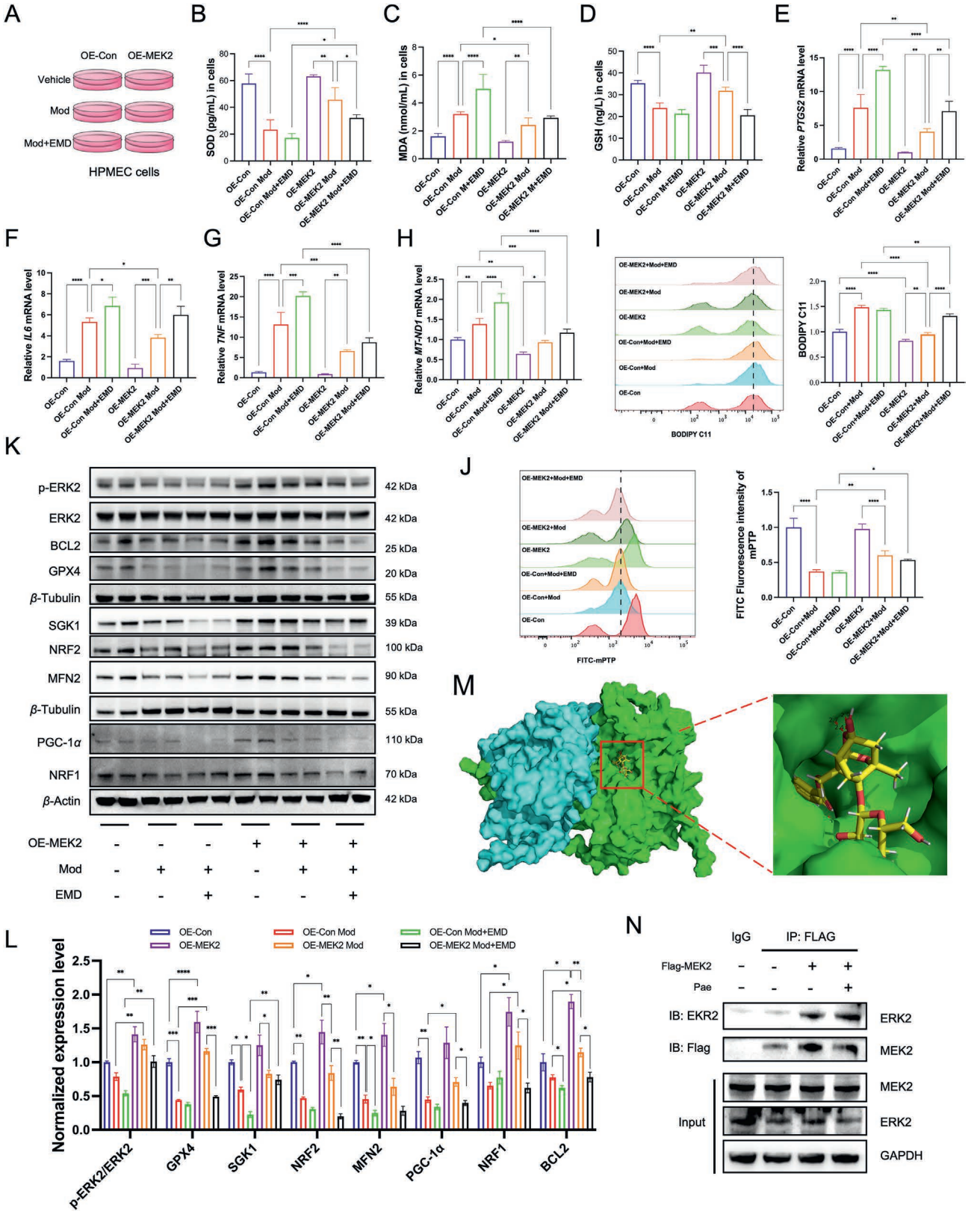

Figure 8 MEK2 overexpression suppresses lipid peroxidation and mPTP opening, and improves mitochondrial biogenesis. (A) Schematic diagram of the cellular experiment process. (B−D) ELISA analysis of cellular oxidative stress indicators (SOD, MDA, GSH) levels (n = 4). (E−H) Q-PCR analysis of intracellular *PTGS2* (E), *IL6* (F), *TNF* (G), and *MT-ND1* (H) mRNA levels (n = 4). (I) Flow cytometry analysis of cellular BODIPY C11 (n = 3−4). (J) Flow cytometry analysis of cellular mPTP (n = 3−4). (K, L) Western blot analysis of cellular p-ERK2, ERK2, BCL2, GPX4, SGK1, NRF2, MFN2, PGC-1α, and NRF1 protein expression (n = 3−4). (M) Molecular docking to analyze the effect of

elevation *in vitro* (Fig. 6B and C). Similarly, U0126 significantly decreased the increase in GSH levels (Fig. 6D) caused by Pae and promoted the upregulation of lipid peroxidation levels in HPMEC cells (Fig. 6E). In addition, Pae significantly reversed the opening of the mPTP induced by U0126 (Fig. 6F and G). This data implied that U0126 causes cellular oxidative stress and mitochondrial damage. To explore the mechanism of Pae, we detected the expression of MEK2, p-ERK2/ERK2, and SGK1 proteins (which may be downstream proteins of ERK2). Intriguingly, U0126 significantly inhibited the effect of Pae on increasing the expression levels of MEK2, p-ERK2 (Fig. 6H and I). Notably, U0126 significantly reduced the effect of Pae on promoting the expression of mitochondrial function-related proteins (PGC-1α, NRF1, NRF2) (Fig. 6H and I), but had no significant effect on OPA1, MFN2 and SGK1 proteins (Fig. 6H and I). Subsequently, we also analyzed apoptosis and ferroptosis-related protein levels. U0126 significantly suppressed the effects of Pae up-regulation of GPX4, BCL2 and Pae down-regulation of BAX (Fig. 6H and I). As expected, Q-PCR detection also found that U0126 markedly decreased *SGK1* (Fig. 6J) and *GPX4* mRNA levels (Fig. 6K). These data indicate that MEK2 inhibition induces cellular oxidative stress and mitochondrial damage, abrogating Pae's protective effects.

3.7. Knockdown of MEK2 causes mitochondrial damage, induces mPTP opening and aggravates lipid peroxidation in vitro

To further confirm MEK2's role in Pae's protective effects, MEK2 was silenced in HPMECs using *MEK2* siRNA (si-MEK2) (Fig. 7A). Q-PCR and Western blot verified successful MEK2 knockdown (Supporting Information Fig. S5A and S5B). MEK2 knockdown significantly reduced Pae-induced GSH and SOD levels and increased MDA content (Fig. 7B−D), indicating impaired antioxidant capacity. Q-PCR showed that MEK2 knockdown decreased *MEK2* and *SGK1* mRNA (Fig. S5C and S5D), and enhanced the levels of *PTGS2, IL1B*, and *IL6* mRNA (Fig. 7E−G). Meanwhile, mitochondrial mtDNA content (MT-ND1, MT-ND4) can indirectly reflect mitochondrial damage[37]. Q-PCR results showed that knockdown of MEK2 significantly upregulated *MT-ND1*, and *MT-ND4* mRNA levels and eliminated the inhibitory effect of Pae (Fig. 7H, Fig. S5E). This suggests that MEK2 knockdown causes mitochondrial damage. To examine the effect of MEK2 knockdown on mitochondrial damage, it was shown by flow cytometry and confocal fluorescence assay that MEK2 knockdown significantly aggravated hypoxia-induced lipid peroxidation (Fig. 7I) and excessive opening of mPTP *in vitro* (Fig. 7J and K).

To confirm the improving effect of Pae on lung injury was dependent on the MEK2−ERK2 pathway, Western blot analysis of the expression of related proteins was performed. As expected, MEK2 knockdown significantly suppressed ERK2 protein phosphorylation and decreased SGK1 protein levels (Fig. 7L and M). Further analysis of mitochondrial biogenesis and dynamics related proteins including NRF1, NRF2, MFN2, and OPA1. Knockdown of MEK2 markedly inhibited the expression of NRF1, NRF2, and OPA1 proteins (Fig. 7L and M, Fig. S5B). Pae failed to improve mitochondrial biogenesis and dynamics related proteins in si-MEK2 cells. Similarly, the levels of ferroptosis-associated proteins and mRNA were explored and the enhanced GPX4 caused by Pae were eliminated after MEK2 knockdown (Fig. 7L and M, Fig. S5F). Apoptotic protein and gene expression were also analyzed in HPMEC cells, Pae failed to improve the level of BCL2 and BAX protein/gene in si-MEK2 cells (Fig. 7L and M, Fig. S5G and S5H). Overall, these findings support the idea that the efficacy of Pae in hypobaric hypoxia-induced lung injury depends on MEK2.

3.8. Inhibition of SGK1 induces oxidative stress, promotes mPTP opening, and induces apoptosis and inflammatory responses

Recent studies have shown that SGK1 can maintain MMP and calcium homeostasis by phosphorylating VDAC1 protein and inducing its ubiquitination degradation, thereby inhibiting the abnormal opening of the mPTP[22]. To further determine whether SGK1 is involved in the regulation of Pae's maintenance of mitochondrial homeostasis, we added an SGK1 inhibitor (EMD683638, EMD) to HPMEC cells (Supporting Information Fig. S6A). We examined the effects of EMD on oxidative stress, inflammatory factors, lipid peroxidation, and mPTP opening in HPMEC cells. ELISA results showed that EMD significantly inhibited Pae to ameliorate hypoxia-induced aberrant expression of SOD, MDA, and GSH (Fig. S6B−S6D). Flow cytometry also demonstrated that EMD treatment counteracted Pae's alleviation of lipid peroxidation (Fig. S6E) and excessive opening of mPTP (Fig. S6F) in HPMEC cells. As expected, Q-PCR assay confirmed that EMD significantly increased *IL6*, *TNF*, and *PTGS2* mRNA levels (Fig. S6G−S6I). Similarly, EMD also significantly counteracted Pae's up-regulation of hypoxia-induced reduction in *BCL2* mRNA levels and down-regulation of elevated *BAX* and *CASP3* mRNA levels (Fig. S6J−S6L).

To confirm SGK1 as a downstream target of ERK2, EMD in combination with LM22B (an agonist of ERK2) was used in the HPMEC cells (Fig. S6M). ELISA results showed that EMD significantly abrogated the reversal of aberrant SOD, MDA, and GSH expression by LM22B (Fig. S6N−S6P). Flow cytometry also showed that EMD counteracted the effect of LM22B in hypoxia-induced lipid peroxidation (Fig. S6Q) and mPTP over-opening (Fig. S6R) in HPMEC cells. As expected, Q-PCR analysis confirmed that LM22B significantly inhibited inflammatory responses (Fig. S6S−S6U) and apoptosis (Fig. S6V−S6X), while EMD counteracted the effects of LM22B. This indicates that SGK1 acts as a downstream factor of ERK2, and inhibition of SGK1 can induce oxidative stress and inflammatory responses, promote the opening of mPTP and apoptosis.

3.9. MEK2 overexpression in vitro reduces lipid peroxidation, inhibits mPTP opening, and improves mitochondrial biogenesis

To continue to verify the involvement of MEK2 in the regulation of mitochondrial homeostasis by Pae, MEK2 overexpression (OE-MEK2) was performed in HPMEC cells (Fig. 8A). Western blot confirmed successful overexpression (Supporting Information Fig. S7A and S7B). ELISA analysis revealed that OE-MEK2 in HPMEC cells enhanced antioxidant activity, including SOD, MDA, and GSH (Fig. 8B−D). Q-PCR results showed that the

Pae on the binding of MEK2−ERK2 complex. (N) IP assay for the effect of Pae on MEK2 and ERK2 protein interactions. *P* values are calculated by one-way ANOVA followed by the Tukey's test. Data are presented as mean ± SD; $*P < 0.05$; $**P < 0.01$; $***P < 0.001$; $****P < 0.0001$.

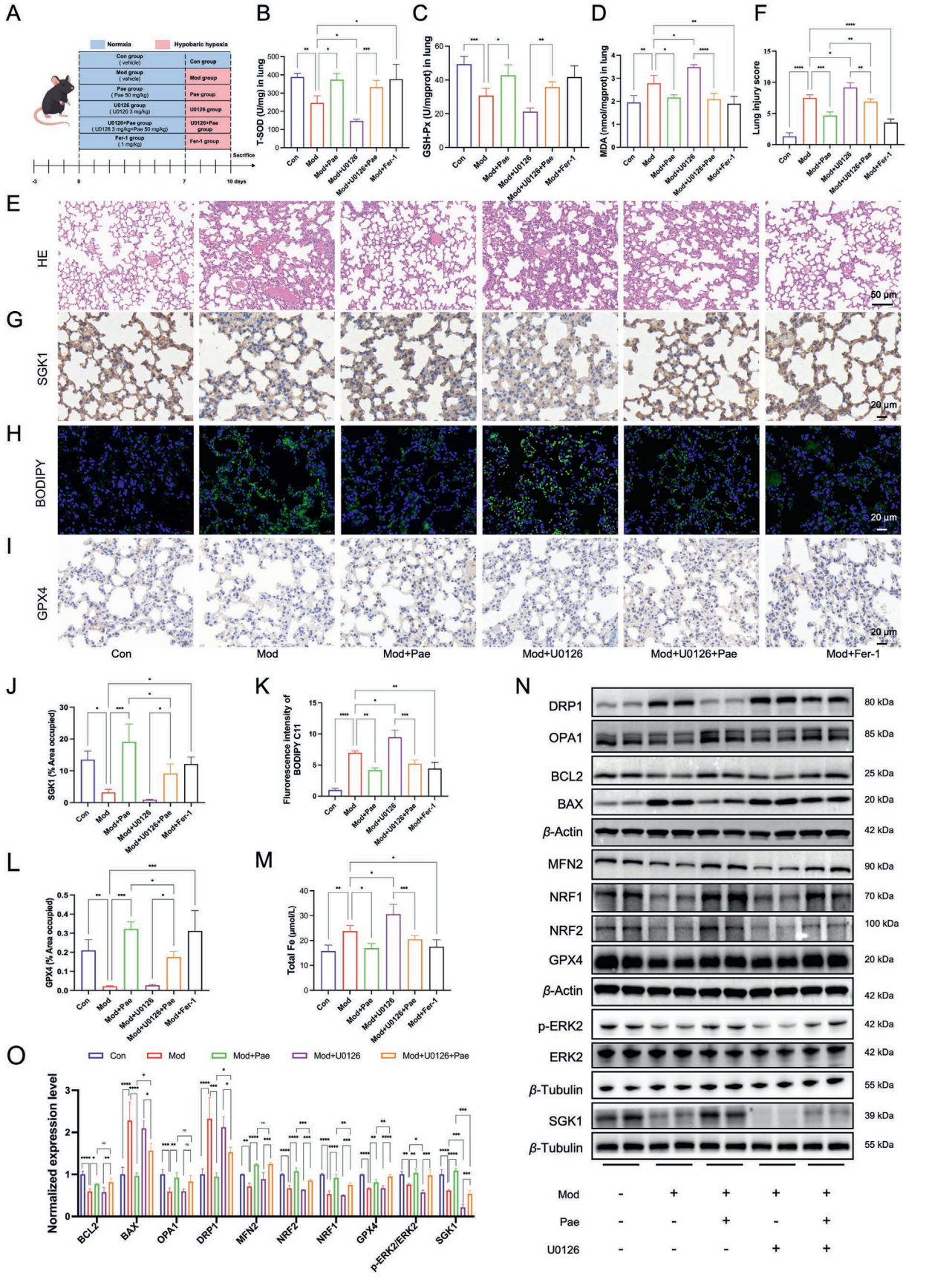

Figure 9 Pae activates the MEK2-ERK2-SGK1 axis *in vivo* to ameliorate mitochondrial dysfunction and alleviate hypobaric hypoxic lung injury. (A) Schematic diagram of the animal experiment. (B−D) ELISA analysis of T-SOD, GSH-Px, and MDA contents in lung tissues

levels of pro-inflammatory factors (*IL6*, *TNF*, and *PTGS2* mRNA) were significantly suppressed in OE-MEK2 cells (Fig. 8E−G). Meanwhile, Q-PCR results revealed that OE-MEK2 significantly down-regulated *MT-ND1*, *MT-ND4* mRNA levels and eliminated the effect of EMD (Fig. 8H, Fig. S7C). This suggests that OE-MEK2 in HPMEC cells reversed EMD-induced mitochondrial damage. Notably, OE-MEK2 also significantly protected HPMEC cells from hypoxia-induced lipid peroxidation (Fig. 8I) and inhibited hypoxia-induced mPTP over-opening (Fig. 8J). In addition, we analyzed the expression of OE-MEK2 on downstream ERK2 and SGK1 proteins. The results revealed that OE-MEK2 significantly upregulated p-ERK2/ERK2 and SGK1 protein expression (Fig. 8K and L). We further analyzed the level of mitochondrial biogenesis and kinetics-related proteins by OE-MEK2. As expected, OE-MEK2 promoted the expression of NRF1, NRF2, MFN2, and PGC-1α protein expression (Fig. 8K and L). Importantly, OE-MEK2 also significantly reversed the inhibitory effects of hypoxia on GPX4, BCL2 protein expression (Fig. 8K and L) and *BCL2*, *BAX*, and *CASP3* mRNA transcription (Fig. S7D−S7F). Interestingly, to determine the regulatory role of Pae on MEK2/ERK2 interaction, we performed molecular docking and IP experiments, respectively. Docking results revealed that the binding of the Pae−MEK2−ERK2 ternary complex was more stable with a binding energy of −9.44 kcal/mol compared to the binding energy of the Pae−MEK2 binary complex (−8.12 kcal/mol). As shown in Fig. 8M and Supporting Information Fig. S8, the MEK2 protein structure is shown in green, the ERK2 protein structure is shown in cyan, and the yellow part in the center is Pae. Apparently, Pae still binds to the MEK2 protein Ser-198 amino acid (Fig. S8). In addition, the IP results also showed that MEK2 bound to ERK2 more obviously after Pae addition (Fig. 8N). These results indicate that MEK2 overexpression mimics Pae's protective effects, and Pae promotes MEK2-ERK2 complex formation to activate downstream signaling.

3.10. Pae activates the MEK2−ERK2−SGK1 axis in vivo to ameliorate mitochondrial dysfunction and alleviate hypobaric hypoxic lung injury

To confirm whether inhibition of the MEK2−ERK2−SGK1 axis exacerbates hypobaric hypoxia-induced lung injury, C57 mice were treated with Pae and U0126 (Fig. 9A). Subsequently, U0126 significantly promoted hypobaric hypoxia-induced inflammatory responses and oxidative stress, as reflected in elevated levels of proinflammatory factors (TNF-α, IL-1β, IL-6) in lung tissue (Supporting Information Fig. S9A−S9C). At the same time, this is also reflected in abnormal oxidative stress indicators (T-SOD, GSH-Px, MDA) in lung tissue and serum (Fig. 9B−D, Fig. S9D−S9F). Consistently, U0126 significantly aggravated inflammatory cell infiltration and alveolar wall thickening in lung tissues of model mice and elevated histopathological scores, while the Pae-treated group showed a significant therapeutic effect (Fig. 9E and F). To further validate the effect of U0126 on the MEK2−ERK2−SGK1 axis, we found by immunohistochemistry that U0126 significantly reduced SGK1 positive expression (Fig. 9G and J). Meanwhile, the results of WB experiments also revealed that inhibition of MEK2 also decreased p-ERK2/ERK2, and SGK1 protein expression (Fig. 9N and O). In addition, we also continued to verify the effect of Pae on U0126 in regulating mitochondrial homeostasis and apoptosis in lung tissues. Western blot experiments revealed that U0126 significantly reduced the expression of Nrf1, Nrf2, and enhenced the level of DRP1, BAX protein (Fig. 9N and O). This aberrant expression of these proteins severely affected mitochondrial function. Pae's intervention treatment significantly reversed the aberrant expression of NRF1, NRF2, DRP1, MFN2, BCL2, and BAX proteins (Fig. 9N and O). To further evaluate the effect of U0126 on ferroptosis in lung tissue, we examined lung tissue lipid peroxidation, total iron and lung tissue GPX4 levels, respectively. It was found that U0126 promoted hypobaric hypoxia-induced lung tissue lipid peroxidation (Fig. 9H and K), GPX4 downregulation (Fig. 9I, L, N, O), and lung tissue total Fe accumulation (Fig. 9M). Notably, Pae succeeded to improve ferroptosis and apoptosis caused by hypobaric hypoxia-induced mitochondrial damage. Consequently, these results reveal that the pulmonary protective effect of Pae depends on MEK2−ERK2−SGK1 axis.

3.11. MAP2K2 knockdown in pulmonary vascular endothelial cells abolished the improvement effect of Pae on lung injury

To further confirm that the beneficial effects of Pae on hypobaric hypoxia-induced lung injury depend on MEK2 *in vivo*, *MAP2K2* gene knockdown (KD) mice in pulmonary vascular endothelial cells was examined using AAV-VEC-Tie1 (Fig. 10A), which were supported by the Western blot and immunohistochemistry analysis (Supporting Information Fig. S10A−S10D). MEK2 KD decreased significantly levels of MPO (Fig. 10B), LDH (Fig. 10C), and COX-2 (Fig. 10D) in hypobaric hypoxia-induced lung injury. MEK2 KD also causes structural changes in the lungs (Fig. 10E and F) and exacerbates inflammatory responses in BALF (Fig. S10E), lung tissue (Fig. S10F), and serum (Fig. S10G−S10I).

In addition, MEK2 KD resulted in an decrease in SGK1 protein expression (Fig. 10G and H) and a significant increase in lipid peroxidation (Fig. 10I and J) in lung tissue. This contributes to the exacerbation of oxidative stress (GSH, MDA, and SOD) (Fig. 10K, Fig. S10J and S10K), iron overload (Fe^{2+}) (Fig. 10L), weakened mitochondrial biogenesis (down-regulating the levels of OPA1, MFN2, NRF1, and NRF2 protein) (Fig. 10M and N), and ultimately leads to endothelial cell apoptosis (BCL2 and BAX protein) and ferroptosis (GPX4 protein) (Fig. 10M and N). Additionally, Pae failed to improve pulmonary structural changes and lipid peroxidation in MEK2 KD mice (Fig. 10E, F, I, J). Meanwhile, Western blot results also revealed that MEK2 KD also decreased p-ERK2/ERK2 (Fig. 10M and N). These data implied that stimulation of ERK2−SGK1 axis by Pae *via* contribution to the MEK2 was not observed in MEK2 KD mice. Notably, the MEK2 KD plus Pae group did not show further improvement in

(n = 4−5). (E, F) Lung histopathology scores with HE pathology staining plots (n = 3). (G, J) Immunohistochemical analysis of the expression of SGK1 in lung tissue (n = 3). (H, K) BODIPY C11 fluorescence analysis of lipid peroxidation levels in lung tissue (n = 3). (I, L) Immunohistochemical analysis of the expression of GPX4 in lung tissue (n = 3). (M) Effect of U0126 on total Fe content in lung tissue (n = 3−4). (N, O) Western blot analysis of the effect of DRP1, OPA1, BCL2, BAX, MFN2, NRF1, NRF2, GPX4, p-ERK2, ERK2, SGK1 protein expression in lung tissues (n = 3−4). P values are calculated by one-way ANOVA followed by the Tukey's test. Data are presented as mean ± SD; *$P < 0.05$; **$P < 0.01$; ***$P < 0.001$; ****$P < 0.0001$; ns: not significant.

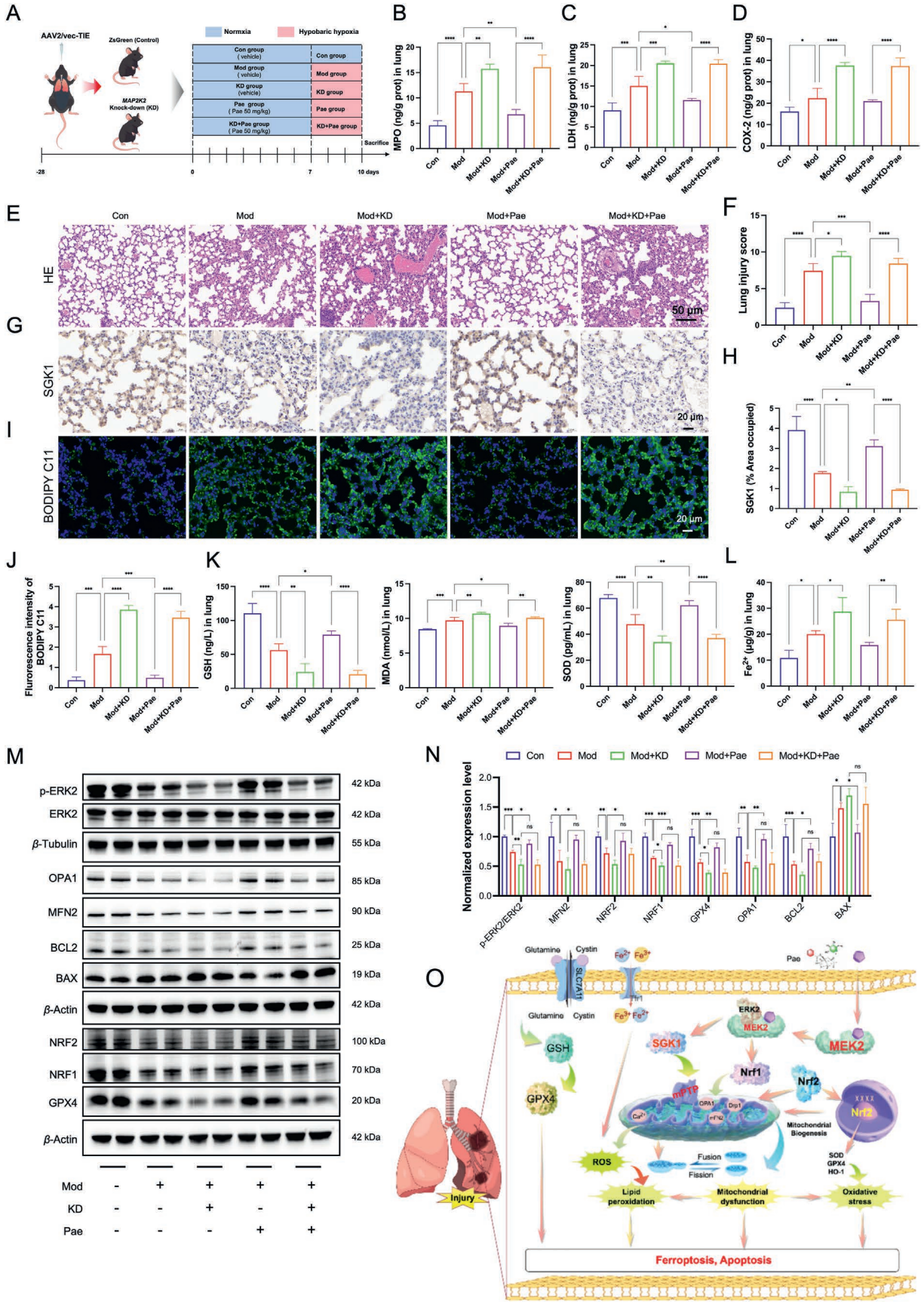

Figure 10 Knockdown of MEK2 in pulmonary vascular endothelial cells abolished the lung injury protective effect of Pae. (A) Schematic diagram of the animal experiment. (B−D) ELISA analysis of MPO, LDH, and COX-2 contents in lung tissues (n = 4−5). (E, F) Lung

mitochondrial function and inhibition of ferroptosis in hypobaric hypoxia-induced lung injury. These results reveal that the pulmonary protective effect of Pae depends on MEK2. All of the above data confirm that Pae binds to MEK2 and regulates the phosphorylation of ERK2, which activates SGK1, promotes mitochondrial biogenesis and mitochondrial dynamics, and attenuates hypobaric hypoxia-induced lung injury (Fig. 10O, by Figdraw).

4. Discussion

4.1. Pae significantly alleviates hypobaric hypoxic-induced lung injury in mice

Hypobaric hypoxic-induced lung injury is a serious hypoxic lung disease that causes a large number of deaths worldwide each year[38,39]. The complexity of hypobaric hypoxia-induced lung injury pathogenesis, spanning dysregulated inflammation, mitochondrial dysfunction, oxidative stress, and novel cell death pathways like ferroptosis[38,40-42]. The natural product Pae has significant antioxidant and anti-inflammatory effects[43] and significantly alleviates brain damage[44], myocardial damage[45], lung injury[46], and liver injury[47] caused by various factors, especially improving respiratory system diseases. The efficacy of Pae in antioxidant injury has drawn considerable attention to the efficacy of Pae in hypobaric hypoxia-induced lung injury[48]. Many studies have shown that Pae plays a crucial role in lung injury caused by various factors. Pae (50 and 100 mg/kg) protects against influenza A virus-induced acute lung injury by decreasing pulmonary edema, and ameliorating histopathological changes in the lungs[49]. However, the effect of Pae on hypobaric hypoxia-induced lung injury needs further study.

Our results showed that Pae (50 mg/kg) reduces lung water content and wet-dry weight ratio, ameliorates lung structural damage, and reverses hypoxia-induced upregulation of inflammatory proteins. Pae also effectively suppresses oxidative stress and lipid peroxidation in HPMEC and lung tissues, which is consistent with lung tissue proteomic data showing reversal of ROS regulatory pathways. These findings support Pae's potential as a therapeutic agent for acute hypobaric hypoxia-induced lung injury.

4.2. Screening and validation of Pae target proteins

Advancements in multi-omics have revealed numerous direct targets of Pae. Proteomics-based screening methods for small molecule target proteins include thermal proteomics[50], DARTS[51], Lip-MS[52], ABPP[53], and the newly developed PELSA technology[54]. Among them, Lip-MS has attracted much attention because it does not rely on exogenous tag synthesis, can fully simulate the binding of small molecule compounds and target proteins under physiological conditions, and is able to identify the binding regions of target proteins. In this study, LiP-MS, molecular docking, MDS, CETSA, DARTS, SPR, MST, and point mutation analysis identified MEK2 as a high-confidence target of Pae, with binding residues at K101, D156, and S198. MEK2 act as a linear relay in the MAPK pathway to mediate development and homeostasis. Studies have shown that MEK2 deficiency leads to the disappearance of ERK2 phosphorylation, triggering weakened cell proliferation and apoptosis[55]. Correspondingly, MEK2 acts as a classical ERK1/2 upstream kinase, and we found that Pae was able to increase the phosphorylation level of ERK2, which in turn activated ERK2 to promote the expression of downstream-related survival molecules. IP results indicated that the enhanced interaction between MEK2 and ERK2 promoted by Pae was the main reason for the activation of ERK2 phosphorylation. Docking results showed that Pae could be more stable by binding to the SER198 site on the MEK2-ERK2 complex. This suggests that Pae binds to Ser198 on MEK2, promotes the interaction of MEK2 with ERK2, and activates ERK2 phosphorylation.

4.3. Pae exerts protective effects against hypobaric hypoxic lung injury through ERK2-SGK1 regulation of mitochondrial homeostasis

Mitochondria in endothelial cells primarily play a signaling role in the cell's response to environmental signals. Mitochondrial homeostasis has an important regulatory effect on angiogenesis, oxidative stress, and inflammatory activation[56]. Hypoxia activates DRP1 phosphorylation, inducing excessive mitochondrial fission, releasing cytochrome C, and promoting apoptosis[36]. Conversely, hypoxia leads to reduced OPA1 protein levels inhibiting mitochondrial fusion, compromising the structural integrity of mitochondrial cristae, and decreasing the efficiency of ATP synthesis[57]. *In vivo* experiments, Pae was able to attenuate the oxidative stress state, ameliorate apoptosis occurring in lung tissues, and reverse mitochondrial homeostatic regulatory proteins in hypobaric hypoxia-induced injury mice. *In vitro* experiments, Pae significantly elevated mitochondrial oxidative phosphorylation function (OCR) and increased MMP. Meanwhile, we found that the regulatory effects of Pae on mitochondrial homeostasis were dependent on the presence of MEK2−ERK2 as well as SGK1. ERK2 and SGK1 as well-known survival molecules regulate mitochondrial homeostasis through multiple pathways[58-60]. Importantly, we found that Pae significantly improved mPTP and reversed the dynamic homeostasis of proteins including mitochondrial division DRP1 as well as fusion OPA1, MFN2, and others by promoting the formation of MEK2−ERK2 complex and subsequent induction of SGK1 expression. Ultimately, mitochondrial dynamic homeostasis was maintained under hypoxia to minimize subsequent excessive apoptotic and inflammatory responses.

histopathology scores with HE pathology staining plots ($n = 3$). (G, H) Immunohistochemical analysis of the expression of SGK1 in lung tissue ($n = 3$). (I, J) BODIPY C11 fluorescence analysis of lipid peroxidation levels in lung tissue ($n = 3$). (K) ELISA analysis of GSH, MDA, and SOD contents in lung tissues ($n = 4-5$). (L) Effect of MEK2 KD on Fe^{2+} content in lung tissue ($n = 3-4$). (M, N) Western blot analysis of the effect of p-ERK2, ERK2, OPA1, MFN2, BCL2, BAX, NRF1, NRF2, and GPX4 protein expression in lung tissues ($n = 3-4$). (O) Schematic representation of the mechanism of Pae's pharmacological activity. Pae binds to MEK2 and regulates the phosphorylation of ERK2, which activates SGK1, promotes mitochondrial biogenesis and mitochondrial dynamics and alleviates hypobaric hypoxia induced-lung injury. *P* values are calculated by one-way ANOVA followed by the Tukey's test. Data are presented as mean ± SD; $^{*}P < 0.05$; $^{**}P < 0.01$; $^{***}P < 0.001$; $^{****}P < 0.0001$; ns: not significant.

4.4. The MEK2−ERK2−SGK1 pathway is essential for Pae to exert its protective effects

ERK2 and SGK1, key mediators of tumor cell survival, regulate apoptosis resistance and mitochondrial homeostasis—mechanisms that support tumor progression[21,61]. However, in this study, they ameliorate hypobaric hypoxia-induced lung injury through survival signaling pathways. SGK1 blocks pro-apoptotic BIM expression by phosphorylating FOXO (promoting cytoplasmic retention and ubiquitin-dependent degradation[62]), enhances PINK1/Parkin-mediated mitophagy[63], and maintains MMP and calcium homeostasis by phosphorylating VDAC1 (inhibiting abnormal mPTP opening)[22]. ERK2 and SGK1 also exhibit synergistic effects: ERK2 phosphorylates GSK3β to inhibit its activity (blocking mitochondrial outer membrane permeability)[64], while SGK1 promotes mitochondrial biogenesis *via* PGC-1α activation, ensuring energy supply under hypoxia[65]. MEK2 knockdown *in vivo* and *in vitro* suppressed the level of p-ERK2 and SGK1 protein, abolished the improvement effect of Pae on hypobaric hypoxia-induced lung injury. These data implied that MEK2−ERK2−SGK1 pathway is essential for Pae to exert its pulmonary protective effects.

5. Conclusions

In this study, we demonstrate that the MEK2−ERK2−SGK1 signaling axis is critical for Pae's pharmacological activity. Using MEK2 inhibitors, MEK2 knockdown (*in vivo* and *in vitro*), and MEK2 overexpression (*in vitro*), we confirm that Pae's pulmonary protective effects are MEK2-dependent. Collectively, our findings show that Pae activates MEK2, inhibits mPTP opening *via* the ERK2−SGK1 axis, maintains mitochondrial homeostasis, and effectively alleviates hypobaric hypoxia-induced lung injury. These results highlight Pae's potential as a therapeutic agent for hypoxic lung injury-related diseases.

Data availability

All proteomic data involved in this study have been submitted to the ProteomeXchange Consortium through the iProX repository partner[66] with the accession code PXD060005. The above datasets of raw data can be accessed *via* the following links and passwords: https://www.iprox.cn/page/PSV023.html;?url=1744244485918xcNS, password: 6qzL.

Acknowledgements

This work was supported by the National Natural Science Foundation of China (82204774), and Innovation Team and Talents Cultivation Program of National Administration of Traditional Chinese Medicine (ZYYCXTD-D-202207, China).

Author contributions

Zhenhui Wu: Writing - Original Draft, Methodology, Validation, Investigation. Yihao Wang: Conceptualization, Writing - Review & Editing, Funding acquisition. Renjie Wang: Data Curation, Resources, Investigation. Rong Gao: Investigation. Shubei Li: Formal analysis. Bodan Tu: Investigation. Xiubing Yin: Investigation. Maoxing Li: Data Curation. Wei Zhou: Investigation. Huanhua Xu: Resources. Zhenfeng Wu: Investigation. Zengchun Ma: Data Curation. Xianglin Tang: Data Curation. Chengrong Xiao: Investigation. Yue Gao: Project administration, Supervision, Writing - Review & Editing.

Conflicts of interest

No conflict of interest was reported by the authors.

Appendix A. Supporting information

Supporting information to this article can be found online at https://doi.org/10.1016/j.apsb.2025.12.024.

References

1. Richalet JP, Jeny F, Callard P, Bernaudin JF. High-altitude pulmonary edema: the intercellular network hypothesis. *Am J Physiol Lung Cell Mol Physiol* 2023;**325**:L155−73.
2. Scherrer U, Rexhaj E, Jayet PY, Allemann Y, Sartori C. New insights in the pathogenesis of high-altitude pulmonary edema. *Prog Cardiovasc Dis* 2010;**52**:485−92.
3. Woods P, Alcock J. High-altitude pulmonary edema. *Evol Med Public Health* 2021;**9**:118−9.
4. Tian L, Zhao C, Yan Y, Jia Q, Cui S, Chen H, et al. Ceramide-1-phosphate alleviates high-altitude pulmonary edema by stabilizing circadian ARNTL-mediated mitochondrial dynamics. *J Adv Res* 2024;**60**:75−92.
5. Fröhlich S, Boylan J, McLoughlin P. Hypoxia-induced inflammation in the lung: a potential therapeutic target in acute lung injury?. *Am J Respir Cell Mol Biol* 2013;**48**:271−9.
6. Madjdpour C, Jewell UR, Kneller S, Ziegler U, Schwendener R, Booy C, et al. Decreased alveolar oxygen induces lung inflammation. *Am J Physiol Lung Cell Mol Physiol* 2003;**284**:L360−7.
7. Eltzschig HK. Targeting hypoxia-induced inflammation. *Anesthesiology* 2011;**114**:239−42.
8. Li Y, Cao Y, Xiao J, Shang J, Tan Q, Ping F, et al. Inhibitor of apoptosis-stimulating protein of p53 inhibits ferroptosis and alleviates intestinal ischemia/reperfusion-induced acute lung injury. *Cell Death Differ* 2020;**27**:2635−50.
9. Pena E, El Alam S, Siques P, Brito J. Oxidative stress and diseases associated with high-altitude exposure. *Antioxidants* 2022;**11**:267.
10. Liao Y, Chen Z, Yang Y, Shen D, Chai S, Ma Y, et al. Antibiotic intervention exacerbated oxidative stress and inflammatory responses in SD rats under hypobaric hypoxia exposure. *Free Radic Biol Med* 2023;**209**:70−83.
11. Xian H, Watari K, Sanchez-Lopez E, Offenberger J, Onyuru J, Sampath H, et al. Oxidized DNA fragments exit mitochondria *via* mPTP- and VDAC-dependent channels to activate NLRP3 inflammasome and interferon signaling. *Immunity* 2022;**55**:1370−85.e8.
12. Zhang P, Zhong D, Yu Y, Wang L, Li Y, Liang Y, et al. Integration of STING activation and COX-2 inhibition *via* steric-hindrance effect tuned nanoreactors for cancer chemoimmunotherapy. *Biomaterials* 2024;**311**:122695.
13. Su L, Zhang J, Gomez H, Kellum JA, Peng Z. Mitochondria ROS and mitophagy in acute kidney injury. *Autophagy* 2023;**19**:401−14.
14. Chen CW, Su C, Huang CY, Huang XR, Cuili X, Chao T, et al. NME3 is a gatekeeper for DRP1-dependent mitophagy in hypoxia. *Nat Commun* 2024;**15**:2264.
15. Chitra L, Boopathy R. Adaptability to hypobaric hypoxia is facilitated through mitochondrial bioenergetics: an *in vivo* study. *Br J Pharmacol* 2013;**169**:1035−47.
16. Chen J, Wang YX, Dong MQ, Zhang B, Luo Y, Niu W, et al. Reoxygenation reverses hypoxic pulmonary arterial remodeling by inducing smooth muscle cell apoptosis *via* reactive oxygen species-mediated mitochondrial dysfunction. *J Am Heart Assoc* 2017;**6**:e005602.

17. Shi J, Yu T, Song K, Du S, He S, Hu X, et al. Dexmedetomidine ameliorates endotoxin-induced acute lung injury *in vivo* and *in vitro* by preserving mitochondrial dynamic equilibrium through the HIF-1a/HO-1 signaling pathway. *Redox Biol* 2021;**41**:101954.
18. Islam MN, Gusarova GA, Das SR, Li L, Monma E, Anjaneyulu M, et al. The mitochondrial calcium uniporter of pulmonary type 2 cells determines severity of acute lung injury. *Nat Commun* 2022;**13**:5837.
19. Roskoski R. ERK1/2 MAP kinases: structure, function, and regulation. *Pharmacol Res* 2012;**66**:105−43.
20. Won M, Park KA, Byun HS, Kim YR, Choi BL, Hong JH, et al. Protein kinase SGK1 enhances MEK/ERK complex formation through the phosphorylation of ERK2: implication for the positive regulatory role of SGK1 on the ERK function during liver regeneration. *J Hepatol* 2009;**51**:67−76.
21. Kashatus JA, Nascimento A, Myers LJ, Sher A, Byrne FL, Hoehn KL, et al. Erk2 phosphorylation of Drp1 promotes mitochondrial fission and MAPK-driven tumor growth. *Mol Cell* 2015;**57**:537−51.
22. Zhou B, Kreuzer J, Kumsta C, Wu L, Kamer KJ, Cedillo L, et al. Mitochondrial permeability uncouples elevated autophagy and lifespan extension. *Cell* 2019;**177**:299−314.e16.
23. Fang L, Zhang M, Li J, Zhou L, Tamm M, Roth M. Airway smooth muscle cell mitochondria damage and mitophagy in COPD *via* ERK1/2 MAPK. *Int J Mol Sci* 2022;**23**:13987.
24. Liu W, Wang X, Liu Z, Wang Y, Yin B, Yu P, et al. SGK1 inhibition induces autophagy-dependent apoptosis *via* the mTOR−Foxo3a pathway. *Br J Cancer* 2017;**117**:1139−53.
25. Zhang X, Zhai Y, Yuan J, Hu Y. New insights into Paeoniaceae used as medicinal plants in China. *Sci Rep* 2019;**9**:18469.
26. Liu Z, Gao J, Ban Y, Wan TT, Song W, Zhao W, et al. Synergistic effect of paeoniflorin combined with luteolin in alleviating lipopolysaccharides-induced acute lung injury. *J Ethnopharmacol* 2024;**327**:118022.
27. Li L, Wang H, Zhao S, Zhao Y, Chen Y, Zhang J, et al. Paeoniflorin ameliorates lipopolysaccharide-induced acute liver injury by inhibiting oxidative stress and inflammation *via* SIRT1/FOXO1a/SOD2 signaling in rats. *Phytother Res* 2022;**36**:2558−71.
28. Ritchie ME, Phipson B, Wu D, Hu Y, Law CW, Shi W, et al. limma powers differential expression analyses for RNA-sequencing and microarray studies. *Nucleic Acids Res* 2015;**43**:e47.
29. Wu T, Hu E, Xu S, Chen M, Guo P, Dai Z, et al. clusterProfiler 4.0: a universal enrichment tool for interpreting omics data. *Innovation* 2021;**2**:100141.
30. Xu M, Xu H, Lin Y, Sun X, Wang L, Fang Z, et al. LECT2, a ligand for Tie1, plays a crucial role in liver fibrogenesis. *Cell* 2019;**178**:1478−92.
31. Nicklin SA, Buening H, Dishart KL, de Alwis M, Girod A, Hacker U, et al. Efficient and selective AAV2-mediated gene transfer directed to human vascular endothelial cells. *Mol Ther* 2001;**4**:174−81.
32. Wang D, Tai PWL, Gao G. Adeno-associated virus vector as a platform for gene therapy delivery. *Nat Rev Drug Discov* 2019;**18**:358−78.
33. Barthez M, Xue B, Zheng J, Wang Y, Song Z, Mu WC, et al. SIRT2 suppresses aging-associated cGAS activation and protects aged mice from severe COVID-19. *Cell Rep* 2025;**44**:115562.
34. Cen M, Ouyang W, Zhang W, Yang L, Lin X, Dai M, et al. MitoQ protects against hyperpermeability of endothelium barrier in acute lung injury *via* a Nrf2-dependent mechanism. *Redox Biol* 2021;**41**:101936.
35. Li X, Zhang W, Xing Z, Hu S, Zhang G, Wang T, et al. Targeting SIRT3 sensitizes glioblastoma to ferroptosis by promoting mitophagy and inhibiting SLC7A11. *Cell Death Dis* 2024;**15**:168.
36. Duan C, Liu R, Kuang L, Zhang Z, Hou D, Zheng D, et al. Activated Drp1 initiates the formation of endoplasmic reticulum-mitochondrial contacts *via* Shrm4-mediated actin bundling. *Adv Sci (Weinh)* 2023;**10**:e2304885.
37. Kleefeld F, Horvath R, Pinal-Fernandez I, Mammen AL, Casal-Dominguez M, Hathazi D, et al. Multi-level profiling unravels mitochondrial dysfunction in myotonic dystrophy type 2. *Acta Neuropathol* 2024;**147**:19.
38. Wang R, Ma S, Yang J, Luo K, Qian Q, Pan J, et al. Sodium hydrosulfide protects rats from hypobaric-hypoxia-induced acute lung injury. *Int J Mol Sci* 2024;**25**:10734.
39. Lin HJ, Wang CT, Niu KC, Gao C, Li Z, Lin MT, et al. Hypobaric hypoxia preconditioning attenuates acute lung injury during high-altitude exposure in rats *via* up-regulating heat-shock protein 70. *Clin Sci (Lond)* 2011;**121**:223−31.
40. Zeng Y, Cao W, Huang Y, Zhang H, Li C, He J, et al. Huangqi Baihe Granules alleviate hypobaric hypoxia-induced acute lung injury in rats by suppressing oxidative stress and the TLR4/NF-κB/NLRP3 inflammatory pathway. *J Ethnopharmacol* 2024;**324**:117765.
41. Yang X, Li J, Ma Y, Dong X, Qu J, Liang F, et al. Curcumin-mediated enhancement of lung barrier function in rats with high-altitude-associated acute lung injury *via* inhibition of inflammatory response. *Respir Res* 2024;**25**:354.
42. Chen J, Zhu H, Chen Q, Yang Y, Chen M, Huang J, et al. The role of ferroptosis in chronic intermittent hypoxia-induced lung injury. *BMC Pulm Med* 2022;**22**:488.
43. Zhang L, Wei W. Anti-inflammatory and immunoregulatory effects of paeoniflorin and total glucosides of paeony. *Pharmacol Ther* 2020;**207**:107452.
44. Zhi SM, Cui Y, Liu Y, Zhang JT, Li XJ, Sheng B, et al. Paeoniflorin suppresses ferroptosis after traumatic brain injury by antagonizing P53 acetylation. *Phytomedicine* 2024;**133**:155940.
45. Ren S, Wang Y, Zhang Y, Yan P, Xiao D, Zhao Y, et al. Paeoniflorin alleviates AngII-induced cardiac hypertrophy in H9c2 cells by regulating oxidative stress and Nrf2 signaling pathway. *Biomed Pharmacother* 2023;**165**:115253.
46. Cheng L, Xiang S, Yu Q, Yu T, Sun P, Ye C, et al. Paeoniflorin inhibits PRAS40 interaction with Raptor to activate mTORC1 to reverse excessive autophagy in airway epithelial cells for asthma. *Phytomedicine* 2024;**134**:155946.
47. Deng X, Li Y, Chen Y, Hu Q, Zhang W, Chen L, et al. Paeoniflorin protects hepatocytes from APAP-induced damage through launching autophagy *via* the MAPK/mTOR signaling pathway. *Cell Mol Biol Lett* 2024;**29**:119.
48. Lu Y, Yin L, Yang W, Wu Z, Niu J. Antioxidant effects of Paeoniflorin and relevant molecular mechanisms as related to a variety of diseases: a review. *Biomed Pharmacother* 2024;**176**:116772.
49. Yu W, Zeng M, Xu P, Liu J, Wang H. Effect of paeoniflorin on acute lung injury induced by influenza A virus in mice. Evidences of its mechanism of action. *Phytomedicine* 2021;**92**:153724.
50. Zeng X, Wei T, Wang X, Liu Y, Tan Z, Zhang Y, et al. Discovery of metal-binding proteins by thermal proteome profiling. *Nat Chem Biol* 2024;**20**:770−8.
51. Lomenick B, Hao R, Jonai N, Chin RM, Aghajan M, Warburton S, et al. Target identification using drug affinity responsive target stability (DARTS). *Proc Natl Acad Sci U S A* 2009;**106**:21984−9.
52. Malinovska L, Cappelletti V, Kohler D, Piazza I, Tsai T-H, Pepelnjak M, et al. Proteome-wide structural changes measured with limited proteolysis-mass spectrometry: an advanced protocol for high-throughput applications. *Nat Protoc* 2023;**18**:659−82.
53. Luo P, Liu D, Zhang Q, Yang F, Wong YK, Xia F, et al. Celastrol induces ferroptosis in activated HSCs to ameliorate hepatic fibrosis *via* targeting peroxiredoxins and HO-1. *Acta Pharm Sin B* 2022;**12**:2300−14.
54. Li K, Chen S, Wang K, Wang Y, Xue L, Ye Y, et al. A peptide-centric local stability assay enables proteome-scale identification of the protein targets and binding regions of diverse ligands. *Nat Methods* 2025;**22**:278−82.
55. Scholl FA, Dumesic PA, Barragan DI, Harada K, Bissonauth V, Charron J, et al. Mek1/2 MAPK kinases are essential for mammalian development, homeostasis, and Raf-induced hyperplasia. *Dev Cell* 2007;**12**:615−29.
56. Kluge MA, Fetterman JL, Vita JA. Mitochondria and endothelial function. *Cir Res* 2013;**112**:1171−88.

57. Liu L, Wu J, Lu C, Ma Y, Wang J, Xu J, et al. WTAP-mediated m6A modification of lncRNA Snhg1 improves myocardial ischemia-reperfusion injury *via* miR-361-5p/OPA1-dependent mitochondrial fusion. *J Transl Med* 2024;**22**:499.
58. Yang L, Luo C, Chen C, Wang X, Shi W, Liu J. All-*trans* retinoic acid protects against doxorubicin-induced cardiotoxicity by activating the ERK2 signalling pathway. *Br J Pharmacol* 2016;**173**:357−71.
59. Li H, Cong X, Sui J, Jiang Z, Fu K, Huan Y, et al. Baicalin enhances the thermotolerance of mouse blastocysts by activating the ERK1/2 signaling pathway and preventing mitochondrial dysfunction. *Theriogenology* 2022;**178**:85−94.
60. Mason JA, Cockfield JA, Pape DJ, Meissner H, Sokolowski MT, White TC, et al. SGK1 signaling promotes glucose metabolism and survival in extracellular matrix detached cells. *Cell Rep* 2021;**34**:108821.
61. Sang X, Han J, Wang Z, Cai W, Liao X, Kong Z, et al. SGK1 suppresses ferroptosis in ovarian cancer *via* NRF2-dependent and -independent pathways. *Oncogene* 2024;**43**:3335−47.
62. Zhang S, Wang Y, Yu M, Shang Y, Chang Y, Zhao H, et al. Discovery of herbacetin as a novel SGK1 inhibitor to alleviate myocardial hypertrophy. *Adv Sci (Weinh)* 2022;**9**:e2101485.
63. Zhao W, Zhao B, Meng X, Li B, Wang Y, Yu F, et al. The regulation of MFG-E8 on the mitophagy in diabetic sarcopenia *via* the HSPA1L−Parkin pathway and the effect of D-pinitol. *J Cachexia Sarcopenia Muscle* 2024;**15**:934−48.
64. Tang X, Li G, Shi L, Su F, Qian M, Liu Z, et al. Combined intermittent fasting and ERK inhibition enhance the anti-tumor effects of chemotherapy *via* the GSK3β−SIRT7 axis. *Nat Commun* 2021;**12**:5058.
65. Jiang D, Fu C, Xiao J, Zhang Z, Zou J, Ye Z, et al. SGK1 attenuates oxidative stress-induced renal tubular epithelial cell injury by regulating mitochondrial function. *Oxid Med Cell Longev* 2019;**2019**:2013594.
66. Ma J, Chen T, Wu S, Yang C, Bai M, Shu K, et al. iProX: an integrated proteome resource. *Nucleic Acids Res* 2019;**47**:D1211−7.